AER P1068

Final project report on

Controlling the Global Weather

by **Ross N. Hoffman, Christopher Grassotti, John M. Henderson, S. Mark Leidner, George Modica, and Thomas Nehrkorn**

For the period **1 March 2002 - 31 March 2004**

Under NIAC subcontract **07600-086**

Submitted to

Universities Space Research Association (USRA)
NASA Institute for Advanced Concepts (NIAC)
Submitted by

Atmospheric and Environmental Research, Inc.
131 Hartwell Avenue, Lexington, MA 02421-3126
Telephone: 781.761.2288
Fax: 781.761.2299

15 July 2004

[This page intentionally left blank.]

EXECUTIVE SUMMARY

One day mankind may be capable of controlling the weather on a global scale. The key factor enabling control of the weather is that the atmosphere is sensitive to small perturbations. Extreme sensitivity to initial conditions suggests that small perturbations to the atmosphere may effectively control the evolution of the atmosphere if the atmosphere is observed and modeled sufficiently well.

It is shown that four-dimensional variational analysis (4d-VAR) is a data assimilation technique that has promise for calculating optimal perturbations for weather modification. Experiments described here demonstrate the ability of 4d-VAR to calculate perturbations to influence the future path of a simulated tropical cyclone. In "target" experiments, the Penn State/NCAR Mesoscale Model 5 4d-VAR system determines the optimal atmospheric state trajectory which simultaneously minimizes the size of the initial perturbation and the difference (using a quadratic norm) between the new model state and a target in which the simulated cyclone has been repositioned. In experiments for Hurricane Iniki, the simulated hurricane was successfully repositioned after the 6 h 4d-VAR period, and then continued on a track parallel to its original track missing the Island of Kauai. Perturbations to the initial conditions are small relative to the hurricane.

In "damage cost function" experiments, 4d-VAR simultaneously minimizes the size of the initial perturbation and an estimate of property loss that depends on wind speed. We had anticipated that the damage cost function would also have the effect of steering the hurricane away from built up areas, but this did not occur. Instead the hurricane surface winds decrease over the built up area at landfall. In the results of these experiments it is as if we have succeeded at making the simulated hurricane "blink" its eye at a precisely controlled time. In damage cost function experiments the optimal perturbations usually include quasi-symmetric concentric features centered on the hurricane. It appears that the perturbation evolves as a wave disturbance that propagates to a focus at the hurricane center, and converts the kinetic energy of the hurricane into thermal potential energy at the appropriate time. The hurricane surface winds regenerate soon thereafter, so the effect is that the high intensity winds surrounding the hurricane eye blink off for a short period.

Since the problem we are solving is very nonlinear it is likely multiple solutions exist and other solutions which shift the hurricane track to reduce the damage cost function may exist. However a damage cost function experiment initialized from the solution of the corresponding target cost function experiment did not find a distinct second solution.

The prototype experiments presented here suggest that global weather control will eventually become a reality especially since many of the supporting disciplines will naturally evolve at a rapid pace. It is plausible that two generations from now controlling the global weather may be within the capabilities and resources of several nations, or groups of nations. In the future, NASA's mission may explicitly include mention of research to control the weather for the benefit of mankind.

1 INTRODUCTION

Theoretical and model studies have established that the dynamics governing the atmosphere can be extremely sensitive to small changes in initial conditions (e.g., Rabier et al. 1996). This suggests that the earth's atmosphere is chaotic. Chaos implies sensitivity to small perturbations. In a realistic numerical weather prediction (NWP) model, since small differences in initial conditions can grow exponentially, small but correctly chosen perturbations induce large changes in the evolution of the simulated weather. Current operational NWP practices—including data assimilation, generation of ensembles, and targeted observations—illustrate this daily (Hoffman 2002). A series of perturbations to the atmosphere might therefore be devised to effectively control the evolution of the atmosphere, if the atmosphere is observed and modeled sufficiently well. Hoffman (2002) hypothesized that as we observe and predict the atmosphere with more and more accuracy, we will become able to effect control of the atmosphere with smaller and smaller perturbations. The questions addressed in the present study are how to calculate the optimal perturbations. Theory tells us that perturbations must have a special structure to grow explosively. A butterfly flapping its wings in South America might affect a tornado over Oklahoma two weeks later, but such an occurrence is in the same category as a chimpanzee typing *Hamlet*.

In our experiments we calculate perturbations to control simulation of Hurricanes Iniki and Andrew of 1992. We base our approach on a particular data assimilation method known as 4d-VAR. 4d-VAR determines a small perturbation to the initial estimate of the atmosphere to optimally fit data in a 6 or $12\ \mathrm{h}$ window. Our experiments are idealized both in terms of the simulation of the hurricanes and in terms of the method of control and should be considered prototypes. Our simulations of hurricanes could be improved with more sophisticated physical parameterizations and higher resolution. Further, we introduce perturbations to the model atmosphere as instantaneous changes. In a more realistic simulation the vector of control parameters that is optimized might be a description of the temporal and spatial patterns of feasible forcing. For example, these parameters might describe additional heating supplied to the atmosphere by a space solar power downlink in the 183 GHz water vapor spectral region. In spite of these simplifications, our experiments demonstrate the control of simulated hurricanes. The amount of energy required is very large, but

we find that the perturbations amplitude decreases if we increase the resolution of the simulation system. Sensitivity experiments show in general that increasing degrees of freedom decrease the overall amplitude of the perturbation and that wind perturbations are more effective than others. In addition, downscaling experiments to higher resolution suggests that our results are relatively robust.

Hurricanes are a natural focus for weather control experiments. The motivation to control the weather is especially strong in the case of tropical cyclones. The AMS policy statement "Hurricane Research and Forecasting" (AMS 2000) summarizes the hazards of tropical cyclones over land: loss of life and nearly $5 billion (in 1998 dollars) annually in damage due to the storm surge, high winds and flooding. The economic cost continues to rise due to growing population and wealth in coastal regions. Further, hurricanes fit the profile of our hypothesis: hurricanes are difficult to predict. One reason is that hurricanes are very sensitive to specified initial conditions and boundary conditions, especially the sea surface temperature and topography. Warm sea surfaces provide latent and sensible energy for hurricanes to grow and rough land surfaces drain energy by frictional processes from hurricanes.

There are many possible means to generate perturbations (Hoffman 2002). These range in scale from seeding an individual cloud from a single-engine aircraft to very large space based reflectors. Evidence that cloud seeding experiments enhance rainfall or decrease hail is accumulating but not on a rigorous scientific basis (Garstang et al. 2003), in part because we are unable to accurately predict the precipitation processes in actual (unmodified) clouds. With regard to space based reflectors, the atmosphere is mainly transparent to solar energy except for clouds which mainly reflect solar energy. Thus the principal effect of reflected solar energy is to change the surface temperature. For example, at the beach on a sunny day the temperature of the exposed sand can be quite a bit higher than sand sheltered by an umbrella. However, such a system has little use over the ocean. Over the ocean, solar energy is primarily absorbed by the ocean or reflected by clouds, but due to the high heat capacity of the ocean, it will be difficult to quickly effect changes to ocean surface temperature using solar reflectors. In order to control a hurricane, one plausible approach is to use a space solar power (SSP) system to produce precise heating of the atmosphere. SSP has been proposed as a non-polluting inexhaustible source of energy. SSP would collect solar energy,

and beam it down to earth. A downlink in microwave frequencies chosen so that the atmosphere is transparent would minimize losses due to heating of the atmosphere. For weather control other frequencies would be chosen. Such an energy source could be modulated in time and directed at different locations. In the vertical, the energy deposition and hence heating is controlled by the transmission frequency and by the distribution of absorbing species, mainly water vapor and oxygen. Figure 1 illustrates this.

In Fig. 1 we plot heating rates as a function of altitude for different frequencies in the microwave spectrum for a top of the atmosphere power flux density of $1500\ \mathrm{Wm}^{-2}$. A single nominal-design SSP station might provide $6\ \mathrm{GW}$ of power which would cover an area $2 \times 2\ \mathrm{km}$ at $1500\ \mathrm{Wm}^{-2}$. The heating rates are calculated for radiation vertically incident at the top of a standard tropical atmosphere. MonoRTM, a very accurate line-by-line radiative transfer model, is first used to calculate transmissivities ($\tau(z)$) every $0.5\ \mathrm{km}$ of altitude (z). These transmissivities increase monotonically from the top of the atmosphere to the surface and energy not transmitted through a layer is deposited in that layer. Thus heating rates may be calculated as

$$\frac{dT}{dt} = -\frac{F_0}{C_p \rho(z)} \frac{d\tau(z)}{dz}. \tag{1}$$

Here T is temperature, t is time, F_0 is the flux at the top of the atmosphere, C_p is the specific heat of air, and ρ is the density of air. There are four major absorption bands in the microwave spectrum: the 22 GHz water vapor band, the 60 and 118 GHz oxygen bands, and the 183 GHz water vapor band. Figure 1a shows that while oxygen and water both absorb strongly, the absorption by the oxygen occurs mainly at levels in the atmosphere high above the bulk of the troposphere. The 183 GHz water vapor band presents the greatest opportunity to apply heating to the troposphere ($\sim 0 - 12\ \mathrm{km}$). Since water vapor in the atmosphere is very variable, the heating profiles will be a function of the meteorology, but this variation could be included in calculating the optimal orientation and power of the downlink. The 183 GHz band allows the vertical distribution of the heating to be controlled by tuning the transmission frequency in this part of the spectrum. This can be seen more clearly in Fig. 1b which shows heating rate profiles for selected frequencies near 183 GHz. As the frequency approaches 183 GHz the atmosphere becomes more opaque and more energy is absorbed at higher levels.

While SSP is a plausible system to control the atmosphere by heating, the prototype experiments reported here do not directly correspond to SSP. Instead, for this study we considered instantaneous changes to the atmospheric state. We explored allowing different variables to change, restricting the region where changes are allowed, and variations in the goal of the optimization. In some experiments we determine changes to the temperature structure of the atmosphere—closely related to but surely not the same as heating of the atmosphere. In one of these experiments we exclude changes to the temperature of the central part of the hurricane—an option we wished to examine since rain drops strongly absorb 183 GHz radiation. Our methods could be extended so that the control variables describe heating as a function of time and position instead of the atmospheric state. A further extension would use frequency and intensity of radiation at the top of the atmosphere as control variables. Ultimately a model of the SSP station would be added and the control variables for the optimization would be the actual control parameters determining the power, frequency, and orientation of the downlink.

2 THE 4d-VAR METHOD

For weather forecasting, 4d-VAR finds the smallest perturbation at the start of each data assimilation period so that the solution best fits all the available data. 4d-VAR solves this complex nonlinear minimization problem iteratively, making use of the adjoint of a linearized version of the model. The operational use of 4d-VAR at the European Center for Medium Range Weather Forecasts and Météo France demonstrates the practical control of realistic simulations of the atmosphere. Current 4d-VAR practice finds the smallest global perturbation as measured by the *a priori*, or background, error covariances but it is possible to modify 4d-VAR to find the smallest perturbation measured in some other way. The MM5 implementation of 4d-VAR used in this study is described by Zou et al. (1997). It has been applied to assimilate zenith delay observations from global positioning system (GPS) satellites (De Pondeca and Zou 2001) and to assimilate cloud-cleared brightness temperatures from geostationary operational environmental satellite (GOES) sounders (Zou et al. 2001).

2.1 Target cost function

The experiments reported here are based on variations of 4d-VAR. We first describe our "target" experimental procedure and then our "damage cost function" procedure. In all cases we consider the unperturbed simulation as reality. In a target experiment we seek a controlled state close to the observed state at the initial time ($t = 0$), such that at a later time ($t = T$), the controlled simulation is close to a target state. To mathematically define the objective function that will be minimized by 4d-VAR, we first define the unperturbed simulation U, from time 0 to T, with corresponding states $U(0)$ and $U(T)$. Then, for example, we define the target or goal state $G(T)$ such that the tropical cyclone is repositioned, say 100 km west of the position in $U(T)$. We then use 4d-VAR to find an optimal controlled simulation C by simultaneously minimizing the difference from the target (i.e., $C(T) - G(T)$) and the initial state (i.e., $C(0) - U(0)$). In other words, $C(0) - U(0)$ is the minimal perturbation to get within $C(T) - G(T)$ of the target. To create the target state we use the bogus procedure described below (§ 3.4), with the initial vortex displaced relative to the unperturbed case.

In these preliminary experiments, both the target mismatch and the size of the initial perturbation are represented in the cost function by a simple quadratic norm:

$$J(t) = \sum_{x,k} \frac{1}{S_{xk}^2} \left[\sum_{i,j} \{C_{xijk}(t) - G_{xijk}(t)\}^2 \right] . \tag{2}$$

Here x defines the control vector variables (i.e., the temperature or the horizontal wind components or all variables), $i, j,$ and k index the grid points in the three spatial dimensions, and t denotes time (either 0 or T). In target experiments we use 4d-VAR to minimize the sum $J(0) + J(T)$. Note that to apply Eq. (2) to $t = 0$, we define $G(0) = U(0)$, i.e., the goal at $t = 0$ is to stay close to the unperturbed initial conditions. In Eq. (2), the flux or "coupled" form of the variables is used since this is the form of the primitive equations in the MM5. For example, $p_* u$ is the coupled eastward wind component, where p_* is the reference pressure difference between the bottom and top model boundaries. The reference state varies in the vertical only, therefore p_* depends only on the model surface topography. Below, we present the components of $J(t)$ for temperature at different times and model layers as the square root of the terms in square brackets in Eq. (2) for x equal to temperature, normalized by the number of grid points, and dimensionalized assuming

$p_* = 950$ hPa, the value over the ocean. The components of $J(t)$ for vector winds, also presented below, are calculated in the same way as for temperature but for the sum of the terms for the horizontal wind components (u, v).

The scales S_{xk} depends only on variable and layer. The scales are used to equalize the contributions of variables of different quantities and magnitudes. Effectively the scales are the relative costs of introducing perturbations at different levels or in different variables. In the present experiments S_{xk} is calculated as the maximum absolute difference between $U(0)$ and $U(\delta t)$ for each variable at each layer, with δt taken to be 40×60 s. Fig. 2 shows the vertical profiles of the S_{xk} used in our experiments, again dimensionalized assuming $p_* = 950$ hPa. In general these scales vary smoothly in the vertical, except that there is a maximum for eastward wind component in the upper troposphere in some cases. The light lines for Iniki correspond to experiment $\mathcal{C}[\boldsymbol{X}_2]$ and for Andrew to experiment $\mathcal{C}[T_a]$ (both described later) and indicate the degree to which scales calculated in this way may be sensitive to the initial state. This discussion would have been simplified if we had simply specified the scales based on *a priori* arguments. However as mentioned in the Introduction the eventual control variables and cost function do not depend on the atmospheric state, but on the parameters describing the perturbations to the system.

2.2 Damage cost function

For the damage cost function experiments the total cost function is defined as

$$J_{\text{total}} = J(0) + \lambda \sum_t J_d(t). \tag{3}$$

Here the subscript d stands for damage and λ is a weighting factor. The damage cost function, J_d, is written in terms of physical damage estimates based on an empirical relationship between surface wind speeds and economic damage. The contribution to the cost function at each grid point is the product of the fractional wind damage (D_{ij}) and the property value (P_{ij}). Thus,

$$J_d(t) = \sum_{i,j} D_{ij}(t) P_{ij}. \tag{4}$$

The property values are unitless. The fractional damage (Unanwa et al. 2000) depends upon two threshold wind speeds; the lower threshold (U_0) is the wind speed at which damage to property first

occurs, while the second (U_1) is the wind speed at which complete destruction occurs. Between these two threshold values, we model the increase in damage using a cosine curve

$$D(t) = \frac{1}{2}\left[1 + \cos\left(\pi \frac{U_1 - U(t)}{U_1 - U_0}\right)\right], \tag{5}$$

where $U(t)$ is the simulated horizontal wind speed. Note that U and hence D vary with location. In addition, the thresholds U_0 and U_1 might vary depending on property type at each grid point. In our basic experiments, Eq. (4) and Eq. (5) are evaluated only at time T (at the end of the 4d-VAR interval). In other experiments we evaluate D and J_d every 15 minutes for the last $2\ \mathrm{h}$ of the 4d-VAR interval and sum the contributions. In all cases $\mathrm{U}_0 = 25\ \mathrm{m\ s^{-1}}$ and $\mathrm{U}_1 = 90\ \mathrm{m\ s^{-1}}$. We experimented with the weighting factor λ; results presented here use $\lambda = 400\,000$.

2.3 Control vector

The control vector is a list of all the quantities that are allowed to be varied by the minimization. An example of an element of the control vector is the temperature at a particular grid point. In principle, one could minimize J with respect to the entire model state vector (that is, all prognostic variables at all grid points). For the MM5 these are the three dimensional fields of p_*u, p_*v, p_*T, p_*q, p', and p_*w (coupled eastward and northward wind components, temperature, and specific humidity, perturbation pressure, and coupled vertical velocity, respectively). In some versions of 4d-VAR all variables are allowed to vary even though only temperature, horizontal wind, and humidity observations are used. In such systems an additional constraint may be included in J to control the excitation of gravity waves. In other data assimilation systems p' and w, and perhaps q, are not allowed to vary. We experimented with several different control vectors.

In addition to choosing which variables to include in the control vector, we selectively controlled the geographic regions within the model domain which is allowed to vary. Results presented here include a “quasi-annular” shape (a hollow rectangle or “donut”).

3 EXPERIMENTAL PROCEDURES

We study Hurricanes Iniki and Andrew of 1992 using the Penn State/NCAR Mesoscale Model 5 (MM5) 4d-VAR-system. MM5 produces very detailed and accurate simulations of tropical cyclones when high resolution and advanced physical parameterizations are used (e.g., Liu et al. 1999; Tenerelli and Chen 2001). However, in the current experiments, coarser, $20\ \mathrm{km}$ resolution is used for computational efficiency in most of the work reported here. For the purpose of our demonstration, the unperturbed MM5 simulation is taken to be reality.

3.1 Hurricanes Iniki and Andrew

Central Pacific Hurricane Iniki (1992) caused extensive damage to property and vegetation on parts of the Hawaiian Islands and killed six people (CPHC 1992; Lawrence and Rappaport 1994). The storm made landfall on Kauai at 0130 UTC 12 September 1992, with a central pressure of $945\ \mathrm{hPa}$. Maximum sustained winds over land were estimated at $60\ \mathrm{m\ s^{-1}}$ with gusts as high as $80\ \mathrm{m\ s^{-1}}$. Iniki would have caused less wind damage on the Hawaiian Islands if it had tracked farther west by as little as $100\ \mathrm{km}$ and this observation is the basis for some of our experiments. For Iniki our experiments calculate optimal perturbations at 0600 UTC 11 September 1992.

Hurricane Andrew (1992) was extraordinary in several respects. Damage was in the tens of billions of dollars, a quarter of a million people were left homeless, and dozens of people died either directly or indirectly. Andrew made landfall in southern Florida near Homestead AFB at 0900 UTC 24 August with a central pressure of $922\ \mathrm{hPa}$ and surface winds gusting to $70\ \mathrm{m\ s^{-1}}$ (Wakimoto and Black 1994; Willoughby and Black 1996). Andrew crossed southern Florida in about $4\ \mathrm{h}$. Our experiments for Andrew calculate optimal perturbations at 0600 UTC 23 August 1992 and at 0000 UTC 24 August 1992. Surface pressure decreased very rapidly in the $48\ \mathrm{h}$ leading up to 0000 UTC 24 August 1992.

3.2 Mesoscale model

The MM5 used in our experiments is described by Grell et al. (1994) and by Dudhia (1993). In our experiments, the MM5 computational grid covers an approximately $400 \times 400\ \mathrm{km}$ horizontal

domain with ten "sigma" layers in the vertical from the surface to $50\ \mathrm{hPa}$ (or $100\ \mathrm{hPa}$ for the Andrew experiments). The tropical cyclones remain far enough from the domain edges that boundary effects are small during the course of the experiments. The sigma coordinate system is a terrain-following normalized pressure coordinate system (Holton 1992, section 10.3.1). The MM5 may be configured in many ways. However, only simple parameterizations of surface fluxes, radiative transfer, and cumulus convection are currently available in the MM5 4d-VAR system. Except as noted all experiments described here use nonhydrostatic dynamics, a 60 second time step and a $20\ \mathrm{km}$ stereographic grid. The physical parameterizations include the MRF PBL and the Anthes Kuo convection scheme. Large-scale stable (i.e., nonconvective) precipitation occurs whenever a layer reaches saturation. Excess moisture rains out immediately with no re-evaporation as it falls. Long wave radiation is using simple radiative cooling, with cloud effects included. The radiation computation occurs every 30 time steps.

3.3 Data

Data are needed to initialize the MM5 model, and to provide boundary conditions during the 4d-VAR and forecast periods. The boundary conditions define both the model state along the lateral boundaries and surface parameters such as sea surface temperature, land use, and others. From the NCAR archives we obtained the required atmospheric data from NCEP reanalyses (Kalnay et al. 1996), and sea surface temperature (SST) fields from NCEP operational analyses. Other surface parameters were derived from the data bases included in the MM5 distribution.

Figure 3 shows the SST over the entire computational domain for each hurricane. For Iniki the grid is 158×194, while for Andrew it is 200×200. The rectangles within Fig. 3 indicate the domain plotted in all subsequent figures for Iniki and Andrew (except Fig. 29). Topography, land use, and property values used in the computations are shown in Fig. 4. Hurricane Iniki experiments use a basic two-dimensional property value field generated by smoothing topography. The smoother averages all points within $400\ \mathrm{km}$ resulting in a gradient of property values for nearshore water points that aids convergence of the minimizer. In the case of Hurricane Andrew this approach leads to a saddle point in the property value field over south Florida, with higher property values located farther north over Florida and over Cuba, which is not the desired result considering the

actual value of property in south Florida. Therefore for Andrew we also used a refined property value field based on land use (Fig. 25). All urban grid points—which represent built-up cities with high property values—are initially assigned a relative value of 10000; all other grid points are temporarily assigned a value of zero. This initial property value field is then smoothed by averaging all points within $120\ \mathrm{km}$. Land points that still have not been assigned a non-zero value are now set to a value of one. The end result is a property value field which strongly penalizes strong winds ($> 25\ \mathrm{m\ s^{-1}}$) in and near urban areas.

3.4 Hurricane initialization

Available data sets usually only have a hint of an actual hurricane. This is the case for the hurricanes studied here. The use of high resolution satellite data to properly initialize a mesoscale model is an area of ongoing research. Consequently we add an analytic representation of a hurricane vortex using the method of Davis and Low-Nam (2001) $6\ \mathrm{h}$ before the start of our experiments (i.e., at $t = -6$) and let the model representation of the hurricane equilibrate during the $6\ \mathrm{h}$ leading up to the start of the 4d-VAR interval. The Davis and Low-Nam (2001) tropical cyclone bogussing system is part of the MM5 pre-processing procedures and was developed by NCAR and the Air Force Weather Agency (AFWA). Note that before the bogus storm is added the representation of the storm in the original data set is removed. The bogus storm is axisymmetric and is based on specifying the storm position and the radius and magnitude of the maximum wind in the lowest model layer. The maximum wind specified is supposed to represent the average wind speed at the radius of maximum wind speed and might be in the range of 75–90% of the best track wind speed. Given these parameters a Rankine wind vortex is used to generate the bogus lowest model wind field. In a Rankine vortex the wind increases linearly with distance from the storm center to the radius of maximum wind and then decreases following a power law in distance. The exponent used here is $-3/4$. The bogus wind field at upper levels has the same Rankine vortex shape, but the wind speeds decrease according to a specified vertical profile. From the bogus wind field a temperature field is calculated to be in nonlinear, i.e., gradient, balance at all levels. Surface friction is ignored in this process, but the surface winds and other variables adjust within the first $1 - 2\ \mathrm{h}$.

Figure 5 demonstrates the need for, and the effectiveness of, the bogus procedure. The top row

of panels shows the hurricanes at the start of the 4d-VAR interval in the reanalysis. There is no evidence of a strong storm in either case. The bottom row of panels shows the bogus storm for each case at the same time. The bogus storm was initiated $6\ \mathrm{h}$ earlier. Note in both cases that the bogus vortex is well defined, the wind speeds are high, and already possesses a clear wave number one asymmetry (in azimuth about the storm center). In this plot and in similar plots that follow, the wind speed is color coded according to the Saffir-Simpson scale and a single contour is plotted at $25\ \mathrm{m\ s^{-1}}$, the lowest wind speed that produces damage in our simulations. The Saffir-Simpson scale contains five categories for hurricanes. Tropical cyclones are classified according to the maximum sustained wind reported. Up to $33\ \mathrm{kt}$ ($17.0\ \mathrm{m\ s^{-1}}$), they are called tropical depressions; up to $63\ \mathrm{kt}$ ($32.4\ \mathrm{m\ s^{-1}}$) tropical storms; up to $82\ \mathrm{kt}$ ($42.2\ \mathrm{m\ s^{-1}}$) Category 1 hurricanes; up to $95\ \mathrm{kt}$ ($48.9\ \mathrm{m\ s^{-1}}$) Category 2 hurricanes; up to $113\ \mathrm{kt}$ ($58.1\ \mathrm{m\ s^{-1}}$) Category 3 hurricanes; and up to $135\ \mathrm{kt}$ ($69.5\ \mathrm{m\ s^{-1}}$) Category 4 hurricanes. These speed ranges correspond to the following colors in our wind speed plots: gray (TD), green (TS), yellow (Cat 1), red (Cat 2), blue (Cat 3), and purple (Cat 4).

Due to the coarse resolution and simple parameterized physics used here, our simulations are only crude representations of observed track and intensity. The simulated storms are, in fact, still too weak, and, in the case of Iniki, too far to the west. For Iniki, we found it necessary to bogus the model vortex one degree to the east of the National Hurricane Center's best track position in order for the storm in the unperturbed simulations to track over Kauai as observed. (The best track is the official description of a tropical cyclone based on all available information, collected either in real-time or later.)

4 RESULTS

The experiment names given below refer to both the 4d-VAR analyses and the subsequent MM5 forecasts carried out beginning from the analyses. The forecast using unperturbed initial conditions is denoted $\mathcal{U}$. The 4d-VAR analyses reported here examine the effects of different objective functions, of limiting the variables allowed to change in the analysis, and of excluding the storm environment from the analysis.

4.1 Summary of experiments

A summary of the Iniki experiments is provided in Table 1. For the purpose of this discussion we take one experiment ($\mathcal{T}[\boldsymbol{X}]$) that uses the target cost function and another experiment ($\mathcal{C}[T]$) that uses the property damage cost function as base line experiments. Note that in $\mathcal{T}[\boldsymbol{X}]$ the control vector is the entire model state, indicated by $\boldsymbol{X}$, while in $\mathcal{C}[T]$ the control vector is the temperature field only, indicated by T. Table 1 shows that 4d-VAR is more successful in preventing wind damage at 6 h when all fields are allowed to vary (i.e., when the control vector is $\boldsymbol{X}$). In $\mathcal{C}[T]$ topography based property values are used (Fig. 4). As comparisons several other experiments are described and key results are reported. Experiment $\mathcal{T}[T]$ uses the target cost function but the control vector is the temperature field, while experiment $\mathcal{C}[\boldsymbol{X}]$ uses the property damage cost function but the the control vector is the entire model state. Experiment $\mathcal{C}[T_d]$ ("d" for donut) is identical to $\mathcal{C}[T]$ except that grid points in a square region centered on the hurricane center are excluded from the control vector. Analogs to $\mathcal{C}[T]$ with variations on the control vector are experiments $\mathcal{C}[\boldsymbol{V}]$, $\mathcal{C}[w]$, $\mathcal{C}[q]$, and $\mathcal{C}[p']$—in which the control vector is composed of the horizontal wind components, the vertical velocity, the specific humidity, and the perturbation pressure, respectively. The maximum iterations allowed were 50 for the $\mathcal{T}[\cdot]$ and 10 for the $\mathcal{C}[\cdot]$ experiments. The minimization ended early for the $\mathcal{C}[w]$ and $\mathcal{C}[q]$ cases. In these, the minimizer could not determine a clearly-defined direction in which to proceed after five or six iterations. Finally we repeated experiment $\mathcal{C}[\boldsymbol{X}]$ using the solutions of $\mathcal{T}[\boldsymbol{X}]$ as the initial estimate of the solution. This experiment is denoted $\mathcal{C}[\boldsymbol{X}_2]$.

Experiments for Andrew are listed in Table 2. Experiment $\mathcal{C}[T_a]$ ("a" for Andrew) is analogous to the Iniki experiment $\mathcal{C}[T]$. Experiment $\mathcal{L}[T_a]$ is similar but uses a refined cost function based on land use. The starting time is 0600 UTC 23 August 1992 for experiment $\mathcal{C}[T_a]$ and 0000 UTC 24 August 1992 for experiment $\mathcal{L}[T_a]$.

In the tables we report the final value of the components of $J(0)$ and the initial and final values of J_{total}. Note that the initial values for $J(0)$ are zero except for experiment $\mathcal{C}[\boldsymbol{X}_2]$ in which cases they are equal to the final values of experiment $\mathcal{C}[\boldsymbol{X}]$.

4.2 Target baseline experiment

In experiment $\mathcal{T}[\boldsymbol{X}]$ the target is the result of a short term forecast started from a bogus vortex inserted to the west of the bogus location used to begin the unperturbed simulation $\mathcal{U}$. Figure 6 shows the forecast track of Hurricane Iniki for the unperturbed simulation $\mathcal{U}$ and for experiments $\mathcal{T}[\boldsymbol{X}]$ and $\mathcal{T}[T]$. For reference these tracks are plotted over the target wind speed. The center of the simulated hurricane is plotted as a dot for each hour for $t = 0$ to 24 h. The track in experiment $\mathcal{T}[\boldsymbol{X}]$ exactly crosses the center of the target at 6 h, while the track in experiment $\mathcal{T}[T]$ is positioned only a small distance west of the unperturbed track.

Figure 7 shows the total cost function versus iteration for experiment $\mathcal{T}[\boldsymbol{X}]$ and the individual parts of the cost function at $t = 0$ and 6 h. Note the asymptotic behaviour of the cost function and its components. This indicates a successful minimization.

Table 1 shows that $J(0)$ is dominated by the $\delta\boldsymbol{V}$ and to a lesser extent by δT. Thus we concentrate on the perturbations in these variables. Figure 8 shows the profiles of rms difference in temperature and vector wind between model state and target for experiment $\mathcal{T}[\boldsymbol{X}]$. The components of J are converted into rms differences as described in the discussion of Eq. (2). The rms differences are reduced by a factor of three at $\mathrm{t} = 6$ h in both T and $\boldsymbol{V}$. At the end of the minimization, differences at $\mathrm{t} = 0$ h and $\mathrm{t} = 6$ h are roughly balanced. This is consistent with the fact that both components of the cost function are equally weighted. The δT are evenly distributed at all levels, while the $\delta\boldsymbol{V}$ increase with altitude. Perturbation magnitudes are 1 K and 0.1 m s^{-1}. These results are consistent with the scales used (Fig. 2).

Figure 9 shows the structure of the perturbation for experiment $\mathcal{T}[\boldsymbol{X}]$ for δT and $\delta\boldsymbol{V}$ at 350, 650, and 950 hPa. While experiment $\mathcal{T}[\boldsymbol{X}]$ determines increments for all model variables, the horizontal wind increments are, by far, the largest in magnitude compared to the background values, with values up to 10 m s^{-1}. For orientation the surface pressure is overdrawn in light contours. The scale for temperature is one degree Celsius, and for winds 10 m s^{-1}. Perturbations increase in magnitude with decreasing pressure (increasing altitude), more so for temperature than wind. Wind increments are largest within 250 km of Iniki's center. These wind increments have the effect of rotating the wave number one wind speed structure counterclockwise. The temperature increments are larger at middle and upper levels and have a "ringing" characteristic at all levels

away from Iniki's center, with concentric bands of positive and negative magnitude. At these levels there are similar patterns in the wind increments that result in rings of enhanced convergence and divergence. Increments of scaled variables other than the horizontal wind are considerably smaller in magnitude (Table 1).

Figure 10 shows the evolution of the perturbation for experiment $\mathcal{T}[\boldsymbol{X}]$. Horizontal slices of δT, δw and $\delta \boldsymbol{V}$ at selected levels are shown at 2 h intervals. In this figure and succeeding figures of this type the scales are $6°$C, 1 m s^{-1}, and 20 m s^{-1} for δT, δw, and $\boldsymbol{\delta V}$, respectively. For reference the $\mathcal{U}$ surface pressure field at the appropriate time is overplotted in light contours in each panel. The dipole structure of the perturbation indicates the shift of Iniki's eye to the west. The concentric banded structure in all variables is most evident in the δw fields, and fades with time consistent with the presumed gravity wave identification of this part of the initial perturbation.

Figure 11 shows the surface wind field for the unperturbed simulation $\mathcal{U}$ and for experiments $\mathcal{T}[\boldsymbol{X}]$ and $\mathcal{C}[T]$. Experiment $\mathcal{C}[T]$ is discussed further in the next section. The figure shows that in both experiments, the hurricane has accelerated along its track relative to the unperturbed case. In experiment $\mathcal{T}[\boldsymbol{X}]$ the track is shifted westward. At 4 h the counterclockwise rotation of the wave number one asymmetry is evident. Although the areal extent of the damaging winds (> 25 m s^{-1}) has changed little, significant reductions in peak wind speeds are evident in both experiments at 6 and 8 h and especially at 6 h in experiment $\mathcal{C}[T]$.

4.3 Cost function baseline experiment

Figure 12 shows the cost function versus iteration for experiment $\mathcal{C}[T]$. As was the case in Fig. 7, note again the asymptotic leveling off of the total and component cost functions.

Figure 13 shows the profiles of rms difference of perturbation temperature for $\mathcal{C}[T]$ and for various $\mathcal{T}[\cdot]$ and $\mathcal{C}[\cdot]$ experiments. The components of J are converted into rms differences as described in the discussion of Eq. (2). Compared to those of experiment $\mathcal{T}[\boldsymbol{X}]$, the $\mathcal{C}[T]$ temperature perturbations are larger in magnitude and concentrated in the upper troposphere, where perturbations are typically 0.25 K in magnitude. (The discussion of this figure continues in the next section.)

Figure 14 shows the structure of the perturbation δT at 950, 650, and 350 hPa for experiment

$\mathcal{C}[T]$. Note that the temperature scale is $4°$C compared to $1°$C used in Fig. 9. At 950 hPa, the lowest model level, there is cooling close to the eye and heating to the west. At mid and upper levels there is a complex pattern of stronger heating and cooling. These patterns are not correlated between 650 hPa and 350 hPa. Patterns in the intervening layers show that these features twist and amplify with altitude. As in Fig. 9 there is evidence of a banded structure away from the hurricane center increasing with altitude.

Figure 15 shows the evolution of the perturbation for experiment $\mathcal{C}[T]$. As in Fig. 10, horizontal slices of δT, δw and $\delta \boldsymbol{V}$ at selected levels are shown at 2 h intervals. The structure of the perturbation at 6 h is different. Note the extraordinary changes in all three fields close to the hurricane center. The effect of these changes on the full wind fields (Fig. 11) is to effectively suppress the winds to near or below the critical damaging wind level of 25 m s^{-1} at 6 h, and at 6 h only.

4.4 Multiple solutions?

Because the 4d-VAR problem is nonlinear it is possible that multiple solutions exist. Experiments $\mathcal{C}[\boldsymbol{X}]$ and $\mathcal{C}[\boldsymbol{X_2}]$ examined this possibility, but did not find evidence for multiple solutions. Initially we anticipated that the cost function experiments would also steer Iniki away from the Hawaiian Islands. Instead we find a more direct effect on wind speed. So to see if there is another solution that affects the hurricane track rather than its intensity we conducted experiment $\mathcal{C}[\boldsymbol{X_2}]$ which parallels $\mathcal{C}[\boldsymbol{X}]$ but starts with an initial estimate of the perturbation equal to the solution of experiment $\mathcal{T}[\boldsymbol{X}]$.

Figure 16 shows the structure of the wind perturbation $\delta \boldsymbol{V}$ for experiments $\mathcal{C}[\boldsymbol{X}]$ and $\mathcal{C}[\boldsymbol{X_2}]$. Horizontal slices at 350, 650, and 950 hPa show that the two solutions are essentially identical.

4.5 Temperature sensitivity experiments

We conducted several Iniki experiments that allowed temperature to vary. These include $\mathcal{T}[\boldsymbol{X}]$, $\mathcal{T}[T]$, $\mathcal{C}[\boldsymbol{X}]$, $\mathcal{C}[T]$, $\mathcal{C}[\boldsymbol{X_2}]$, and $\mathcal{C}[T_d]$. Profiles of rms temperature increments for these temperature sensitivity experiments (see Fig. 13) show that the temperature increments are smallest when the control vector is $\boldsymbol{X}$ since fields other than temperature are also adjusted. Comparing $\mathcal{C}[T_d]$ to $\mathcal{C}[T]$,

we see that preventing increments near the storm center results in considerably larger increments away from the storm. In experiment $\mathcal{C}[T]$ there are larger increments at lower levels near the storm center. Since $\mathcal{C}[T_d]$ increments in this part of the domain are necessarily zero, the $\mathcal{C}[T_d]$ rms increments are smaller than those for $\mathcal{C}[T]$ at lower levels, but $\mathcal{C}[T_d]$ more than makes up for this at upper levels.

Figure 17 shows the patterns of perturbation temperature δT at $350\ \mathrm{hPa}$ for these experiments. Plots at other levels are qualitatively similar. First, note that the $\mathcal{C}[T]$ temperature increments are 2-4 times larger than those of $\mathcal{C}[\boldsymbol{X}]$. In $\mathcal{C}[T]$, a large cold temperature increment is present directly over the center of Iniki. These temperature increments are in direct opposition to the "warm core" thermodynamic structure of the hurricane and act to destroy the hurricane in place. This cannot be the case for experiment $\mathcal{C}[T_d]$. The pattern of increments in the $\mathcal{C}[T_d]$ experiment, where increments are allowed, is similar to the corresponding increments in the $\mathcal{C}[T]$ experiment, but in $\mathcal{C}[T_d]$ the amplitude of these increments is much larger. The warming and cooling outside the immediate storm environment is four times larger in $\mathcal{C}[T_d]$ than in $\mathcal{C}[T]$ south and southwest of Iniki's center.

Figure 18 shows the surface wind field at $6\ \mathrm{h}$ for the temperature sensitivity experiments. In all the $\mathcal{C}[\cdot]$ analyses, the extent and intensity of damaging winds (winds $> 25\ \mathrm{m\ s^{-1}}$) were drastically reduced in the hours near the evaluation time of the wind damage cost function, 1200 UTC 11 September. It should be noted that the extent and intensity of the winds increased rapidly in the hours following this time in the $\mathcal{C}[\cdot]$ experiments. Most experiments were extremely successful at limiting the number of grid points with damaging winds at $6\ \mathrm{h}$. In experiments $\mathcal{C}[\boldsymbol{X}]$ (and $\mathcal{C}[\boldsymbol{V}]$ described in the next section) the storm remains nearly stationary for $6 - 9\ \mathrm{h}$. This is followed by a northwesterly motion of the vortex, eventually resulting in the storm passing the latitude of Hawaii much later than in the unperturbed case and much farther west. In some experiments, the sea-level pressure field (which is related to the overall temperature through the depth of the atmosphere) appeared to be temporarily mispositioned with respect to the wind field close to the time of the wind damage cost function evaluation. This effect was most noticeable in experiment $\mathcal{C}[T_d]$.

The $\mathcal{C}[T_d]$ experiment is less successful in reducing wind damage compared to the $\mathcal{C}[T]$ experiment. This is expected since, when allowed, 4d-VAR focuses the increments in the proximity of

the storm; in the $\mathcal{C}[T_d]$, of course, increments in this location are not permitted.

Figure 19 shows the evolution of the perturbation for experiment $\mathcal{C}[T_d]$. Qualitatively there are many similarities between this figure and Fig. 15 at 4 h and beyond, and even at 2 h outside the central "donut" area. Although similar in structure the $\mathcal{C}[T_d]$ increments are noticeably more intense. See especially δT and δw at 4 h. As in Fig. 10, δT, δw and $\delta \boldsymbol{V}$ at selected levels are shown at 2 h intervals. The temperature increments show the inward radial movement of the ring of positive temperature increments. Coincident with the collapse of the ring into a centrally located bubble of warm increments is a sudden and rapid decrease in sea-level pressure because sea-level pressure is proportional to the weight of the atmosphere above, which decreases as temperature increases. The increments temporarily disrupt the wind field at the appropriate time (Fig. 18) but there is a rapid increase in wind speed near the surface after 6 h. Thus, it appears that in experiment $\mathcal{C}[T_d]$, and generally in the successful $\mathcal{C}[\cdot]$ experiments, the kinetic wind energy is temporarily converted into thermal (potential) energy. At the same time that the perturbations focus on the hurricane center, other wave-like perturbations propagate radially outward at greater distances from the storm center.

The surface wind increments $\boldsymbol{\delta V}$, initially identically zero, increase in magnitude and propagate radially inward. Near the storm center at 6 h, the wind increments are very large just west of the center to reduce the hurricane wind speed (the area of most intense wind at 6 h in experiment $\mathcal{U}$ shown in Fig. 11). But there is an area south of the center where the wind speed actually increases (the yellow area in the panel for $\mathcal{C}[T_d]$ in Fig. 18).

4.6 Parameter sensitivity experiments

Based on the experiments using $\boldsymbol{X}$ as the control vector we expect that wind is the most effective variable to perturb (see Table 1). To explore this further we conducted additional sensitivity experiments in which the control vector is restricted to each of $\boldsymbol{V}$, w, q, and p' in turn. It should be noted that the scales used affect the numeric results reported in Table 1, but perturbations calculated in experiments like $\mathcal{C}[T]$ in which a single variable is the control vector are less influenced by the scales. Figure 20 shows the perturbations for these parameter sensitivity experiments. The largest perturbations in each case are near the center of Iniki. Increments of smaller magnitude

typically have a concentric pattern of alternating sign at larger distance from the storm's center. That the larger increments occur at the center of the storm is expected, since hurricanes are largely sustained by physical processes in the storm's eyewall. The concentric patterns appear wave-like, propagating both inward and outward with respect to the hurricane center.

Figure 21 shows the surface wind field at 6 h for the parameter sensitivity experiments. A comparison of the surface wind speed category in the unperturbed simulation (Fig. 11, column 1) with the parameter sensitivity experiments simulations (Fig. 21), shows that, in general, the position of Iniki is farther north and west and that damaging winds are substantially reduced at 6 h, less so in $\mathcal{C}[w]$ and more so in $\mathcal{C}[\boldsymbol{V}]$. In experiment $\mathcal{C}[p']$ it is noteworthy that gravity waves advance from the lateral boundaries at 70 m s^{-1} and interact with the inner environment of the storm at 6 h. Apparently this is the most efficient way for 4d-VAR to weaken the storm under the constraints of experiment $\mathcal{C}[p']$. The presence of strong horizontal wind increments near the center of the storm that are similar in size and form in experiments $\mathcal{C}[\boldsymbol{X}]$ and $\mathcal{C}[\boldsymbol{V}]$ is consistent with the fact that 4d-VAR reduces wind damage most efficiently via changes in the initial horizontal wind field. (Compare Fig. 16 and Fig. 20.) In experiment $\mathcal{C}[q]$ we note that there are isolated regions of supersaturation (relative humidity greater than 100%) that are a consequence of large positive perturbations close to the center of the storm and over the large island of Hawaii (not shown). These strongly supersaturated regions only occur early in the $\mathcal{C}[q]$ simulation.

4.7 Refined property damage cost function

We report results from two experiments for Hurricane Andrew. Our first Andrew experiment, $\mathcal{C}[T_a]$, suggested several refinements including a refined cost function that were then implemented for experiment $\mathcal{L}[T_a]$. Experiment $\mathcal{C}[T_a]$ is analogous to Iniki experiment $\mathcal{C}[T]$. The surface wind field at the start of $\mathcal{C}[T_a]$ is shown in Fig. 5 and at the start of $\mathcal{L}[T_a]$ in Fig. 25.

Figure 22 shows the structure of the perturbation δT at 950, 650, and 350 hPa for experiment $\mathcal{C}[T_a]$. As in Fig. 14 the amplitude of δT increases with altitude, and has the smallest scales and largest magnitudes near the hurricane center. Again a concentric pattern of small amplitude and alternating sign is present away from the center.

Figure 23 shows the evolution of the perturbation for experiment $\mathcal{C}[T_a]$. As in Fig. 15, hori-

zontal slices of δT, δw and $\delta \boldsymbol{V}$ at selected levels are shown at 2 h intervals. While there are many differences in detail the qualitative patterns are similar. In this case the 4 h and 6 h patterns are more similar to each other.

Figure 24 shows the evolution of the surface wind field for the unperturbed simulation $\mathcal{U}_a$ and for experiment $\mathcal{C}[T_a]$. Compared to Fig. 11 the wind speeds are reduced to less damaging speeds throughout the interval $4-8$ h, rather than just at 6 h. By comparing the unperturbed simulation $\mathcal{U}_a$ with $\mathcal{C}[T_a]$, one can see that 4d-VAR followed the path of least resistance as defined by the topography-based property value field (shown in Fig. 4). 4d-VAR weakened the storm at the time required by the optimization (1200 UTC) while Andrew was in the Bahamas. At this time, the region of category 1 winds (on the Saffir-Simpson scale) and, to a lesser extent, the region of damaging winds were restricted on the west side of the storm as it passed over the outer edges of the non-zero property value field. Then, after 1200 UTC, the stronger winds on the unaffected eastern part of the storm (not all of the storm was over the non-zero property value grid points at evaluation time) was advected cyclonically around the storm as it moved generally westward. Andrew approached the mainland faster and made landfall just after 0600 UTC compared to approximately 0800 UTC in the unperturbed case; landfall was also farther north than in $\mathcal{U}_a$. In general, after 1200 UTC, strengthening in $\mathcal{C}[T_a]$ was similar to $\mathcal{U}_a$, however, the strong strengthening of the wind field in $\mathcal{U}_a$ right at landfall was not seen in $\mathcal{C}[T_a]$. But later, on the west side of Florida, $\mathcal{C}[T_a]$ was stronger than $\mathcal{U}_a$!

For Hurricane Andrew experiment $\mathcal{L}[T_a]$ we used land use to define the property values and summed Eq. (4) every fifteen minutes over hours four through six of the 4d-VAR interval. Note that experiment $\mathcal{L}[T_a]$ begins 6 h later than $\mathcal{C}[T_a]$ to ensure that Andrew passes over non-zero property values. Figure 25 shows the land use property values. Examination of the $\mathcal{L}[T_a]$ simulation at five minute intervals shows that the storm's intensity is decreased throughout the time interval 6 to 8 h. However the storm regenerates strong surface winds after 6 h.

Figure 26 shows the structure of the perturbation δT at 950, 650, and 350 hPa for experiment $\mathcal{L}[T_a]$. Again the perturbations are qualitatively similar to the perturbations of our other experiments with concentric banded patterns away from the hurricane center. In this case the larger magnitude small scale structures are most apparent at 650 hPa.

Figure 27 shows the evolution of the perturbation for experiment $\mathcal{L}[T_a]$. Compared to Fig. 23, features in the δT and δw fields near the hurricane center are even smaller scale than in the other cases. The wind increment vectors at 6 h are very large at a very few points.

Figure 28 shows the evolution of the surface wind field for the unperturbed simulation $\mathcal{U}_a$ and for experiment $\mathcal{L}[T_a]$. Compared to the situation 6 h earlier the simulation of Andrew is much less intense. As Andrew advances on the Florida coastline from 4 to 6 h in this experiment the 25 m s^{-1} damaging wind contour folds in on the west side of Andrew to satisfy our requirement to minimize wind damage until 6 h. By 8 h this contour has resumed a more circular shape.

4.8 Robustness of the solution

The Andrew 4d-VAR solution for $\mathcal{L}[T_a]$ and the $t = 0$ $\mathcal{U}_a$ state were also used to initialize high resolution enhanced physics simulations. These runs retain the 10 layer vertical structure, but use a grid that is three times finer in both horizontal directions, i.e., with a resolution of ~ 6.67 km. For convenience we will refer to this as the 7 km grid. An even finer time step of 20 seconds is used.

The experiments described so far are what may be called perfect model experiments in that 4d-VAR and our simulations use exactly the same model of the atmosphere. The 7 km experiments show to what extent a perturbation calculated using one approximation to the atmosphere works in a situation with more realistic dynamics. Thus comparing the result of transplanting the 20 km perturbations into a 7 km simulation is a test of the robustness of our methodology.

Figure 29 shows the surface wind field at 6 h for unperturbed and controlled for 20 km and 7 km simulations. The general characteristics of the pairs of simulated surface wind fields match fairly well. Note especially that the perturbations calculated at 20 km are still effective at 7 km. For this figure both the 20 km and 7 km fields are from simulations with different physical parameterizations than in all previous figures. These 20 km simulations use simpler physics than described in § 3.2. In particular the bulk PBL is used instead of the MRF PBL and there is no parameterization of soil moisture. The high resolution 7 km model simulations use enhanced physics including the advanced Schulz explicit moisture microphysics, the more sophisticated Kain-Fritsch cumulus convection parameterization, the CCM2 radiative shortwave heating and longwave cooling and a

multi-layer soil model.

4.9 Findings from preliminary experiments

We carried out preliminary 4d-VAR experiments analgous to $\mathcal{C}[\boldsymbol{X}]$, $\mathcal{C}[T]$, $\mathcal{C}[T_d]$ at a resolution of $40\ \mathrm{km}$ and with simpler physical parameterizations (fixed soil temperature, no land surface fluxes, and no interactions between clouds and radiation.) Perturbations from these experiments had qualitatively similar characteristics to the experiments already described with concentric rings of positive and negative perturbations peaking in the upper troposphere and large increments near the center of the storm at low levels. In the $40\ \mathrm{km}$ experiments the optimal perturbations are larger in scale with less spatial complexity and noticeably larger (roughly speaking two to three times larger) in magnitude. Compare Fig. 30 to Fig. 13. The range for temperature is more than three times larger in Fig. 30. Note that in Fig. 30 results are plotted for experiment $\mathcal{C}[T_d]$ in black and for a $20\ \mathrm{km}$ experiment similar to $\mathcal{C}[T_d]$ but using the same simplified physics as the $40\ \mathrm{km}$ experiments.

5 THE FUTURE

The preliminary study described here shows that 4d-VAR can be used to calculate "optimal" perturbations to control the track or intensity of a simulated tropical cyclone. Clearly it will be a long time before it is possible to control a tropical cyclone in reality. While the results reported here are preliminary in many aspects, they point the way towards further work. A necessary prerequisite is the ability to forecast tropical cyclones accurately. Beyond this, advances in several technical areas are needed. These are discussed in the following paragraphs.

In addition, a number of problems must be solved in the political, economic, and legal realms. For inhabitants of New Orleans, eliminating a hurricane threat to that city may take precedence over all else, yet farmers in the Mid-West might suffer without the resulting rain. This example shows that many competing factors must be considered in defining the cost function to be optimized. These "side issues" may prove more difficult to overcome than the science and engineering issues.

Items 1, 2, and 3 below relating to the calculation of the perturbations could be usefully exam-

ined now with computer simulations that would naturally follow on this study. Advances in items 4 and 5—improved models and observations of the atmosphere—will occur naturally as we improve NWP. Item 6, the creation of perturbations will require engineering new systems. The last two items—improved observations and the creation of perturbations—will require new space-based assets.

1. **Calculation of realistic perturbations.** Solving for the optimal perturbation using a more realistic model is difficult due to the number of degrees of freedom required to represent the atmosphere adequately and the nonlinear and sometimes discontinuous nature of the physics governing the atmosphere. With higher resolution and more degrees of freedom, effective perturbations are expected to require smaller magnitudes but more detailed structure. Incremental 4d-VAR (Lorenc 1997; Rabier et al. 2000), will allow the most sophisticated physics to be used for the trajectory calculation, but simpler physics for the 4d-VAR calculation. The incremental approach eliminates the need to use full resolution in the linear models, and the use of limited physics eliminates the need to code the adjoint of the most complex packages. These changes can increase the speed of the gradient calculation.

2. **Calculation of feasible perturbations.** The 4d-VAR methodology could be extended for this purpose. A control vector could be developed first in terms of heating perturbations continuous in time over a three- or six-hour period, later in terms of the radiation perturbations at the top of the atmosphere, and finally in terms of the orientation, power, and frequency of the SSP downlink antenna.

3. **Overcoming chaos.** The control must be effected at significant time lags to minimize the size of the perturbations, yet the system is inherently unpredictable at long lead times. In general, theoretical predictability studies (Lorenz 1969) suggest that doubling the resolution of the observations will only increase predictability by an amount similar in magnitude to the timescale of the motions of the smallest resolved phenomena. For example, since the timescale for the evolution of a thunderstorm is smaller than one hour, observing details of individual thunderstorms will improve predictability by no more than one hour. Therefore controlling small-scale phenomena may be difficult.

One approach is to continuously monitor and control the system by adding perturbations regularly. Another approach is to control the environment of the phenomena of interest. This viewpoint has some validity for the case of hurricanes. Internal hurricane dynamics have a time scale of a day or less. This limits how far back in time we can go to calculate optimal perturbations. But hurricane tracks are greatly affected (one could say "steered") by the large scale upper level winds and hurricanes cannot maintain intensity and structure in the presence of environmental vertical wind shear. So, an alternative is to control the large scale wind field several days or even a week in advance to affect the hurricane's path or intensity, or to prevent a hurricane from forming.

4. **Improved numerical weather prediction (NWP).** Projecting future computer and space technology trends is difficult. However, the technical roadmap for improving NWP and data assimilation is well established, and the timing of future progress has been estimated (e.g. ECMWF 1999).

5. **Improved atmospheric observations.** Satellites provide a large volume of information, but not always in the right place, or of the right variable, or sufficiently accurate. New instruments on the Terra, Aqua, and Aura satellites hold the promise to fill some of these gaps. Future space-based lidar sensors should be valuable by providing more direct and very accurate measurements of atmospheric properties including winds.

6. **Creation of perturbations.** Optimal perturbations, while small in amplitude, may be large in scale and require substantial amounts of energy. The costs of controlling a hurricane in our simulation experiments in terms of energy required are enormous. In preliminary experiments we did find that halving the grid size more than halved the energy required. If this trend continues down to sub-kilometer-scales (scales that we would like to use for more accurate forecasting in any case), then control of large-scale weather in the future becomes much more believable.

   Mechanisms do not yet exist to create large scale perturbations. Global weather control is by nature opportunistic. Useful technologies will typically have multiple other primary uses. For example, solar reflectors could be used to increase power from solar electric farms, in-

crease the growing season for agriculture, and provide lighting for arctic cities, and space solar power has electric power generation as its primary mission. Eventually weather perturbations may become a commodity with a Global Weather Control Authority purchasing rights to run wind farms in reverse or to control the downlink frequency of space solar power, or negotiating in real time for modest aircraft flight path changes.

With regard to demonstrating effective control of weather, we first note that in spite of our desire for perfection, observations and predictions are always somewhat uncertain. Modern data assimilation uses estimation theory to treat NWP, whether on the global scale or some smaller scale, in a probabilistic sense. We can keep track of uncertainty with Kalman filters or ensemble methods so that we can tell if the predicted impact of some treatment is small or large compared to the predicted uncertainty. Then, if we also simulate the effect of the perturbation, we can perform significance testing before the weather control activity begins!

Our approach of using accurate calculations of the sensitivity of the atmosphere to determine precise perturbations might also be applied to smaller scales as a demonstration test. With current observation systems, it may be possible to take this approach with cloud scale models in the next several years. Real time applications may be far off since the time scales associated with cloud scales are so small compared to current computation resources. However, for the purpose of weather modification experimentation, one could make a probabilistic forecast, say, for untreated cases and validate these probabilistic forecasts with observations. Then having the capability to make validated probabilistic cloud scale forecasts, it becomes possible to state the significance of the difference between an observed treated result and the corresponding forecast untreated result. Furthermore, if one models the effect of the treatment, then one could also compare a forecast treated case and the untreated observation.

This probabilistic approach could be applied now for simple stratiform rain situations. An optimistic assessment is that it will likely be 5 and perhaps 10 years before the current state of the art for observing and simulating cumulus clouds has advanced enough that the uncertainty of the probabilistic forecast is sufficiently small so that useful conclusions may be drawn. In the time range of 10-20 years, our ability to forecast hurricanes may have advanced so much that we will have sufficient confidence to begin control experiments using aircraft contrails or aircraft-

dispersed surface oils. If successful, such experiments may provide additional impetus to speed the development of space solar power. Active control of the large-scale weather patterns to reduce the severity of droughts, to decrease the number of severe tornadoes, and to reduce damage due to hurricanes, may then become a reality 40-50 years from now.

References

AMS, 2000: Hurricane research and forecasting. *Bull. Am. Meteorol. Soc.*, **81**, 1341–1346.

CPHC, 1992: Tropical cyclones report for the central Pacific. Technical Memorandum NWS-PR-38, Central Pacific Hurricane Center, NOAA, Washington, DC, [http://205.156.54.206/pr/hnl/cphc/pages/hurrclimate.html].

Davis, C. and S. Low-Nam, 2001: The NCAR-AFWA tropical cyclone bogussing scheme. Technical Memorandum, Air Force Weather Agency (AFWA), Omaha, NE, [http://www.mmm.ucar.edu/mm5/mm5v3/tc-report.pdf].

De Pondeca, M. F. V. and X. Zou, 2001: A case study of the variational assimilation of GPS zenith delay observations into a mesoscale model. *J. Applied Meteorol.*, **40**, 1559–1576.

Dudhia, J., 1993: A nonhydrostatic version of the Penn State-NCAR mesoscale model: Validation tests and simulation of an Atlantic cyclone and cold front. *Mon. Weather Rev.*, **121**, 1493–1513.

ECMWF, 1999: A strategy for ECMWF, 1999-2008. Miscellanenous publication, Eur. Cent. for Med. Range Weather Forecasts, Reading, England, 16 pp.

Garstang, M. et al., 2003: *Critical Issues in Weather Modification Research*. National Research Council, National Academy of Sciences, Washington, DC, www.nap.edu/books/0309090539/html/.

Grell, G. A., J. Dudhia, and D. R. Stauffer, 1994: A description of the fifth-generation Penn State/NCAR mesoscale model (MM5). Technical Note 398+1A, NCAR, 122 pp.

Hoffman, R. N., 2002: Controlling the global weather. *Bull. Am. Meteorol. Soc.*, **83**, 241–248.

Holton, J. R., 1992: *An Introduction to Dynamic Meteorology*. Academic, New York, third edition, 511 pp.

Kalnay, E., M. Kanamitsu, R. Kistler, W. Collins, D. Deaven, L. Gandin, M. Iredell, S. Saha, G. White, J. Woollen, Y. Zhu, A. Leetmaa, B. Reynolds, M. Chelliah, W. Ebisuzaki, W. Higgins, J. Janowiak, K. C. Mo, C. Ropelewski, J. Wang, R. Jenne, and D. Joseph, 1996: The NCEP/NCAR 40-year reanalysis project. *Bull. Am. Meteorol. Soc.*, **77**, 437–471.

Lawrence, M. B. and E. N. Rappaport, 1994: Eastern North Pacific hurricane season of 1992. *Mon. Weather Rev.*, **122**, 549–558.

Liu, Y., D.-L. Zhang, and M. K. Yau, 1999: A multiscale numerical study of Hurricane Andrew (1992). Part II: Kinematics and inner-core structures. *Mon. Weather Rev.*, **127**, 2597–2616.

Lorenc, A. C., 1997: Development of an operational variational assimilation scheme. *J. Meteorol. Soc. Japan*, **75**, 339–346.

Lorenz, E. N., 1969: The predictability of a flow which possesses many scales of motion. *Tellus*, **21**, 289–307.

Rabier, F., H. Järvinen, E. Klinker, J.-F. Mahfouf, and A. Simmons, 2000: The ECMWF operational implementation of four-dimensional variational assimilation. I: Experimental results with simplified physics. *Q. J. R. Meteorol. Soc.*, **126**, 1143–1170.

Rabier, F., E. Klinker, P. Courtier, and A. Hollingsworth, 1996: Sensitivity of forecast errors to initial conditions. *Q. J. R. Meteorol. Soc.*, **122**, 121–150.

Tenerelli, J. E. and S. S. Chen, 2001: High-resolution simulations of Hurricane Floyd using MM5 with vortex-following mesh refinement. *14th Conference on Numerical Weather Prediction*, American Meteorological Society, Boston, MA, Fort Lauderdale, Florida, J52–J54.

Unanwa, C. O., J. R. McDonald, K. C. Mehta, and D. A. Smith, 2000: The development of wind damage bands for building. *Journal of Wind Engineering and Industrial Aerodynamics*, **84**, 119–149.

Wakimoto, R. M. and P. G. Black, 1994: Damage survey of hurricane Andrew and its relationship to the eyewall. *Bull. Am. Meteorol. Soc.*, **75**, 189–200.

Willoughby, H. E. and P. G. Black, 1996: Hurricane Andrew in Florida: Dynamics of a disaster. *Bull. Am. Meteorol. Soc.*, **77**, 543–549.

Zou, X., F. Vandenberghe, M. Pondeca, and Y.-H. Kuo, 1997: Introduction to adjoint techniques and the MM5 adjoint modeling system. Technical Note 435-STR, NCAR, Boulder, CO.

Zou, X., Q. Xiao, A. E. Lipton, and G. D. Modica, 2001: A numerical study of the effect of GOES sounder cloud-cleared brightness temperatures on the prediction of Hurricane Felix. *J. Applied Meteorol.*, **40**, 34–55.

TABLES

Table 1: *Hurricane Iniki experiments and cost functions.*
The experiment names in the first column are explained in § 4.1. Columns 2 and 3 give the number of iterations and function evaluations required by the optimization. The initial and final total cost function J_{total} are then listed along with the ratio of the final to initial value expressed as a per cent. Next, the components of the cost function due to the perturbation at the initial time are listed for each model variable. The final three columns list the magnitude of the gradient of the cost function at the start and end of the minimization along with the ratio of the final to initial value expressed as a per cent. As the minimum is approached J_{total} should decrease and the gradient should approach zero. **[iniki]**

	Number of		J_{total}			Final $J(0)$ components					‖Gradient‖		
Experiment	Iter.	Eval.	Initial	Final	%	T	$\boldsymbol{V}$	w	q	p'	Initial	Final	%
$\mathcal{T}[\boldsymbol{X}]$	50	53	24132	3875	16	253	977	0	61	23	127	23	18
$\mathcal{T}[T]$	50	53	24132	12950	54	2054	0	0	0	0	55	23	42
$\mathcal{C}[\boldsymbol{X}]$	10	11	80727	313	0.4	20	259	0	12	12	18255	809	4
$\mathcal{C}[T]$	10	12	80727	3742	5	3167	0	0	0	0	8935	2280	26
$\mathcal{C}[T_d]$	10	12	80727	8551	11	6522	0	0	0	0	7125	1323	19
$\mathcal{C}[\boldsymbol{V}]$	10	12	80727	370	0.5	0	355	0	0	0	14674	943	6
$\mathcal{C}[w]$	4	7	80727	77790	96	0	0	2819	0	0	1367	389	28
$\mathcal{C}[q]$	5	7	80727	30160	37	0	0	0	2306	0	7838	5284	67
$\mathcal{C}[p']$	10	15	80727	5958	7	0	0	0	0	4620	6490	1504	23
$\mathcal{C}[\boldsymbol{X}_2]$	47	67	18163	148	1	8	123	0	10	3	11195	485	4

Table 2: *Hurricane Andrew experiments and cost functions. Columns as in Table 1.* **[andrew]**

	Number of		J_{total}			Final $J(0)$ components					‖Gradient‖		
Experiment	Iter.	Eval.	Initial	Final	%	T	$\boldsymbol{V}$	w	q	p'	Initial	Final	%
$\mathcal{C}[T_a]$	10	19	20258	2127	10	1134	0	0	0	0	5988	2058	34
$\mathcal{L}[T_a]$	10	11	3.17E+08	1.16E+07	4	902	0	0	0	0	575361	23766	4

FIGURES

Fig. 1: *Heating rates (degrees/hour) as a function of frequency (GHz) and height (km). Calculations are for the standard tropical atmosphere assuming vertically incident radiation with power flux density of* $1500\ \mathrm{Wm}^{-2}$*. The whole microwave spectrum and heights to* $25\ \mathrm{km}$ *are shown in (a). Values greater than* $3^{\circ}\ \mathrm{h}^{-1}$ *are reset to that value for plotting. This affects higher levels in the oxygen bands where absorption is strong and density is low. Selected profiles near the 183 GHz water vapor resonance are plotted in (b). Here as height increases, density decreases, so that peak heating rates are larger for more opaque frequencies.*

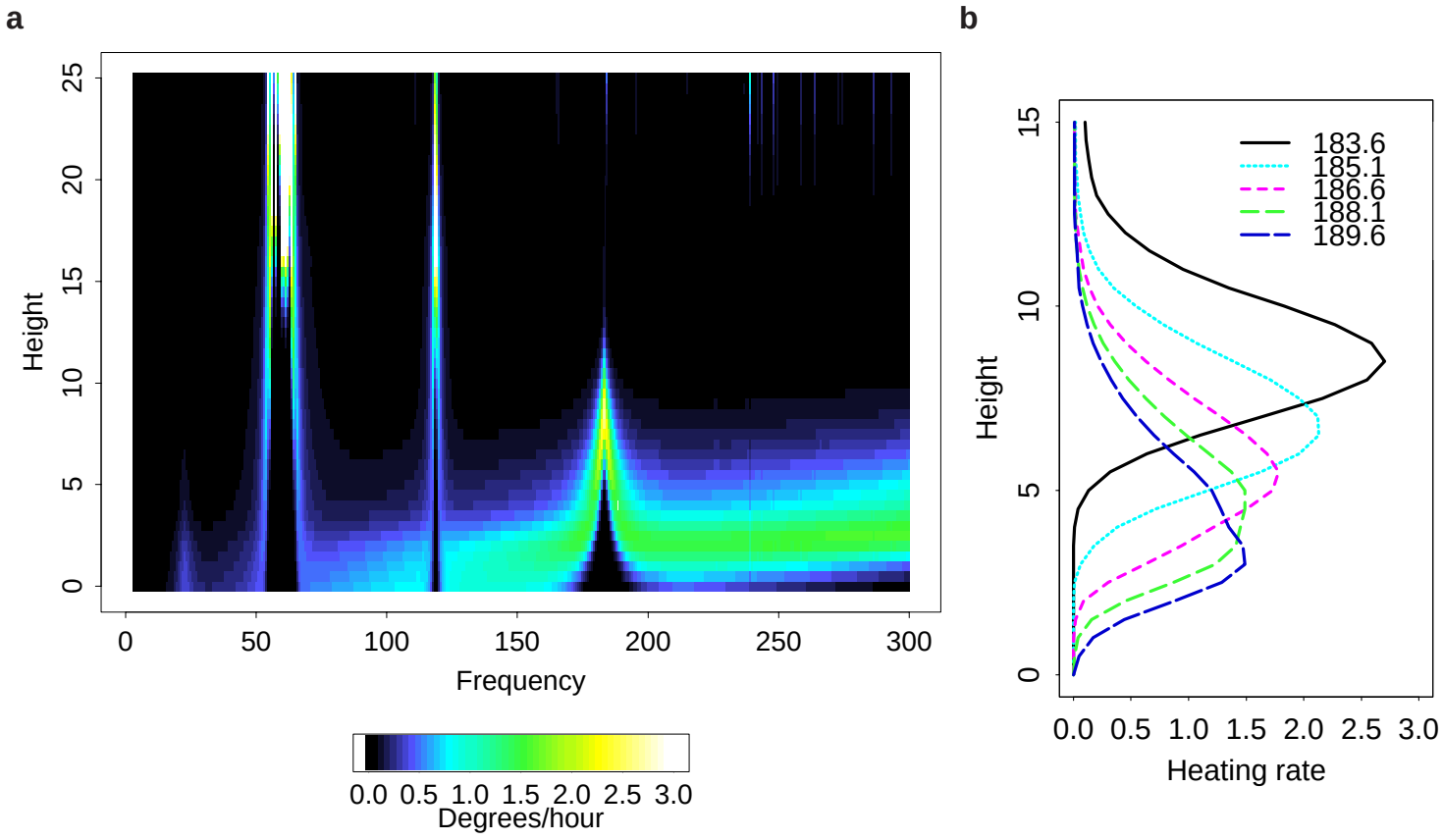

Fig. 2: *Profiles of scaling factors for temperature (T), eastward wind component (u) and northward wind component (v) plotted using solid, dotted, and dashed lines, respectively, for the Iniki and Andrew experiments. Values are calculated from the coupled variables and then dimensionalized for this plot assuming $p_* = 950\,\mathrm{hPa}$. The horizontal scale is degrees Celsius for temperature and $\mathrm{m\ s^{-1}}$ for the wind components. Light lines are for the $\mathcal{C}[\boldsymbol{X}_2]$ and for $\mathcal{C}[T_a]$ experiments described later.*

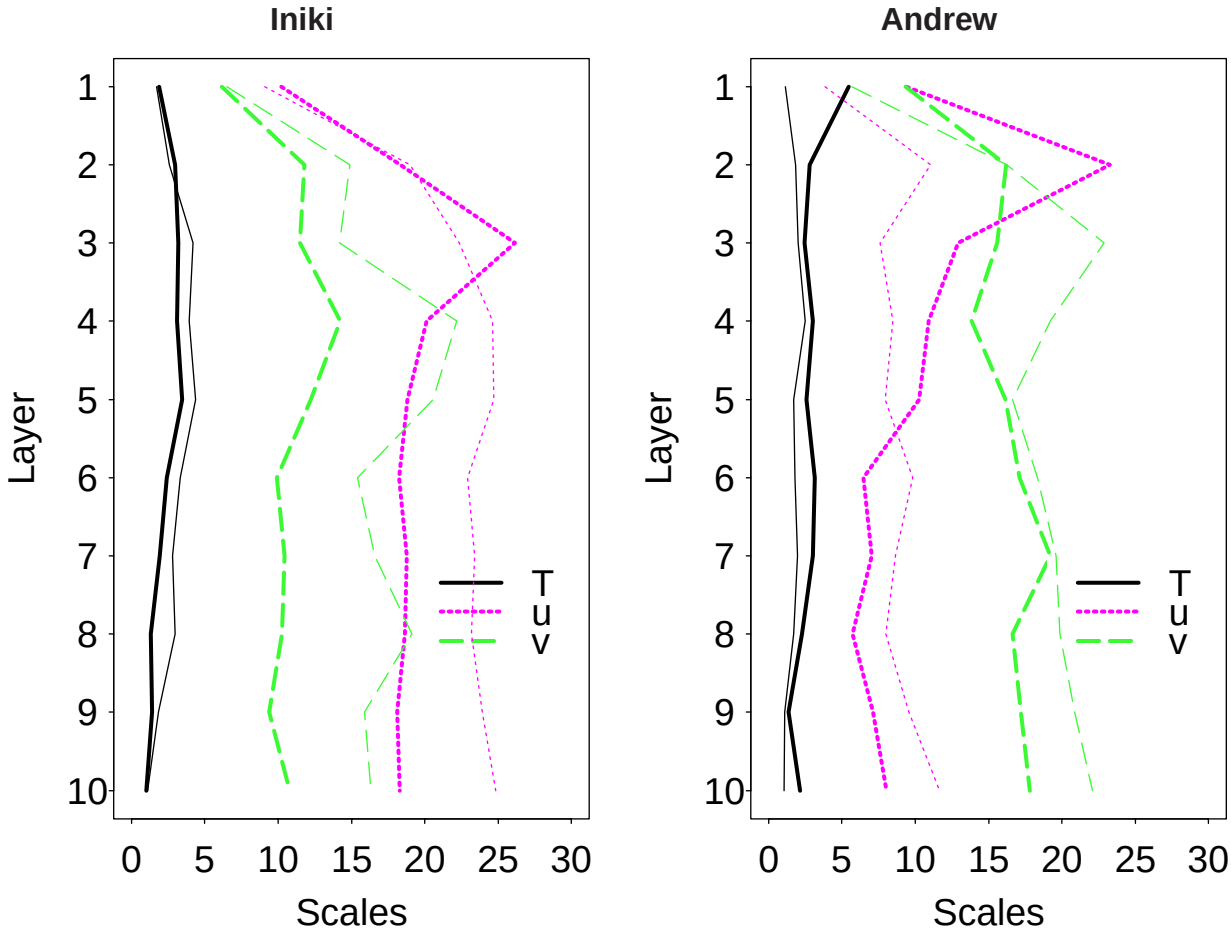

Fig. 3: *Computation domain showing sea surface temperature (SST, degrees Celcius) at the start of the 4d-VAR interval for Iniki and Andrew. The rectangle plotted indicates the area shown in all other figures for Iniki and Andrew.*

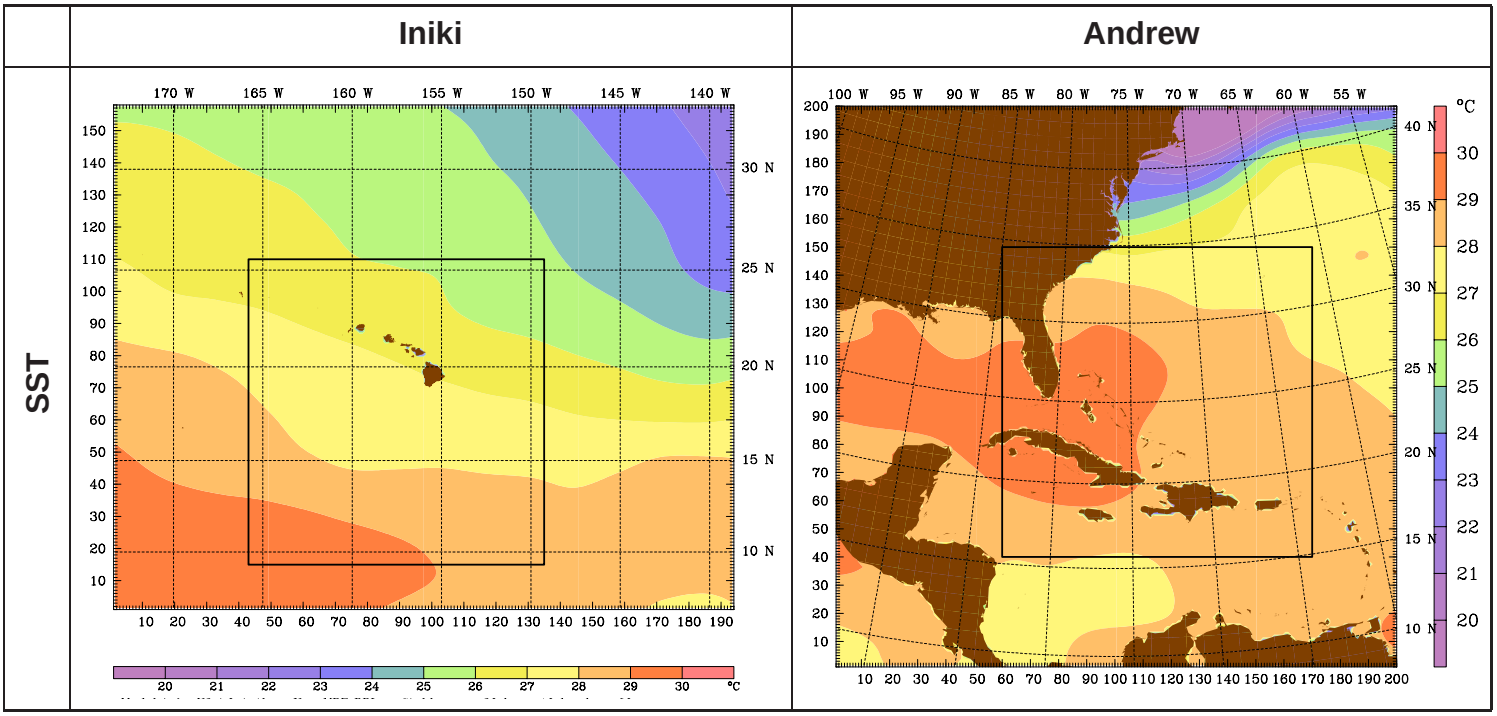

Fig. 4: *Topography, land use, and property values based on smoothing the topography field used in the experiments for Iniki and Andrew. Topography is in meters. Land use is blue for water, different shades of green for crop/woods/grassland, yellow for dryland and irrigated crop/pasture, and black for built up urban areas. Property values are unitless, but might be considered tens of thousands of dollars per square kilometer.*

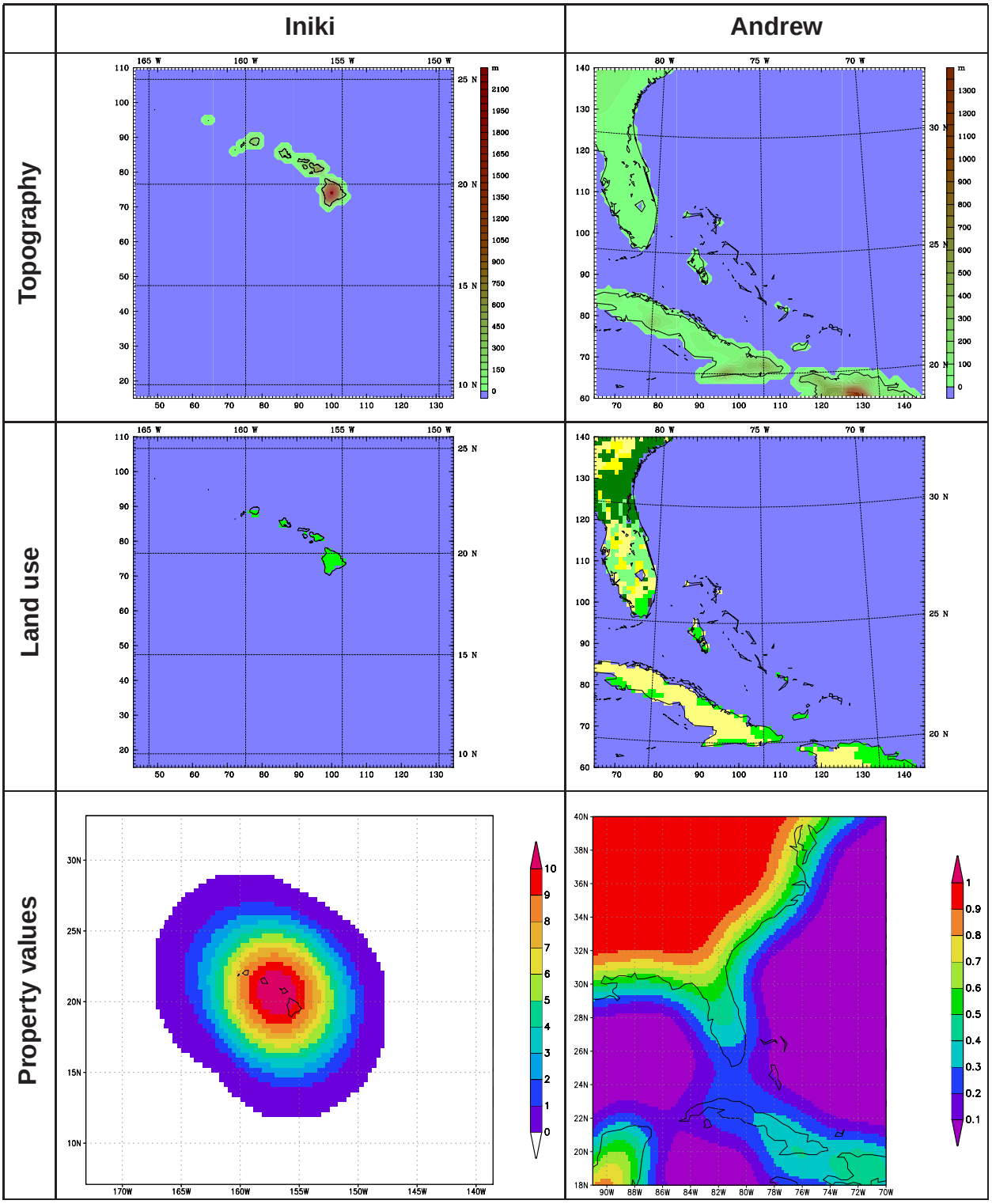

Fig. 5: *Surface pressure and winds at the start of the 4d-VAR interval for Iniki and Andrew as depicted by the reanalysis and bogus procedure. Surface pressure is contoured in* hPa*, wind speed in* $\mathrm{m\ s^{-1}}$ *is color coded, and wind barbs are in kts.*

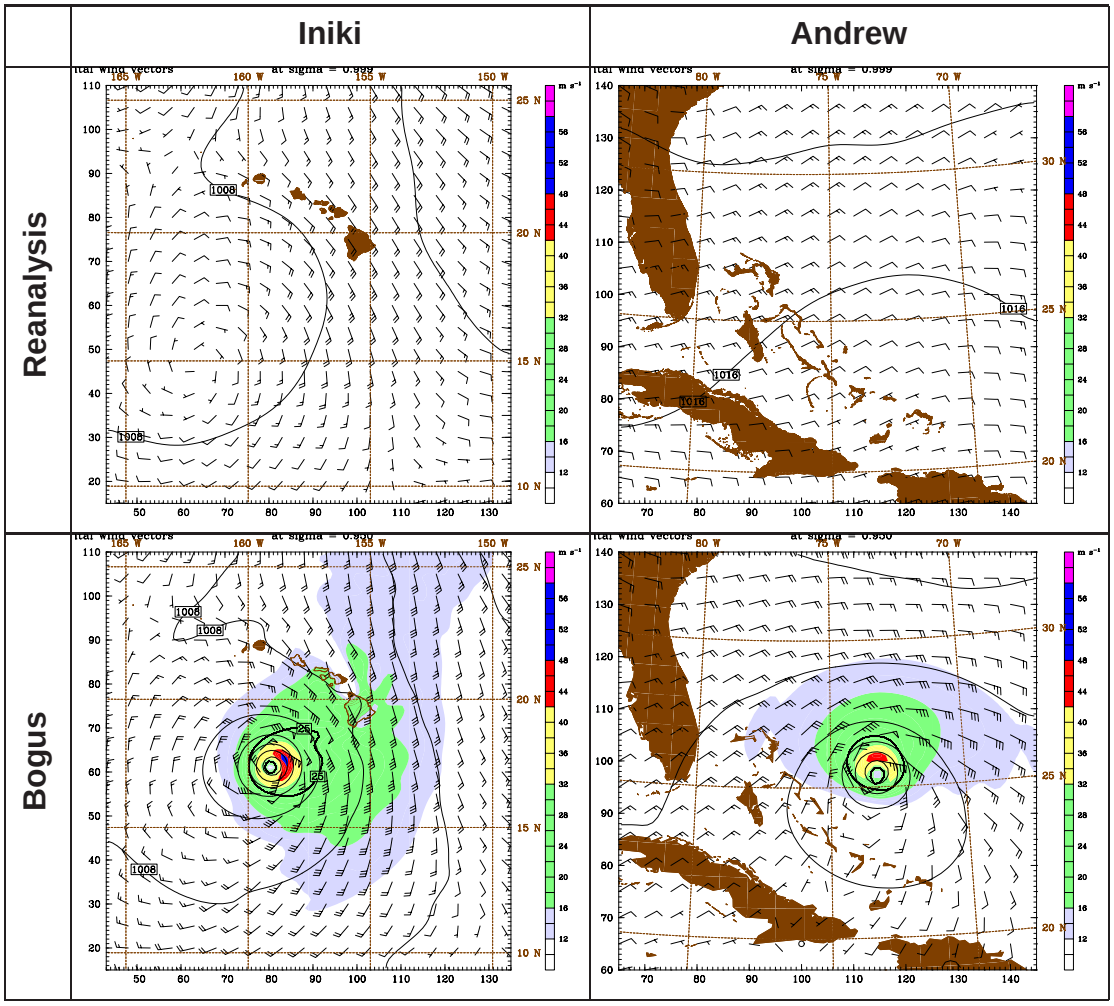

Fig. 6: *The forecast track of Hurricane Iniki is shown for the unperturbed simulation $\mathcal{U}$ and for experiments $\mathcal{T}[\boldsymbol{X}]$ and $\mathcal{T}[T]$. For reference these tracks are plotted over the wind speeds of the repositioned cyclone used as the target. Hourly positions of Iniki are shown as dots, black, orange and dark green for experiments $\mathcal{U}$, $\mathcal{T}[\boldsymbol{X}]$ and $\mathcal{T}[T]$, respectively.*

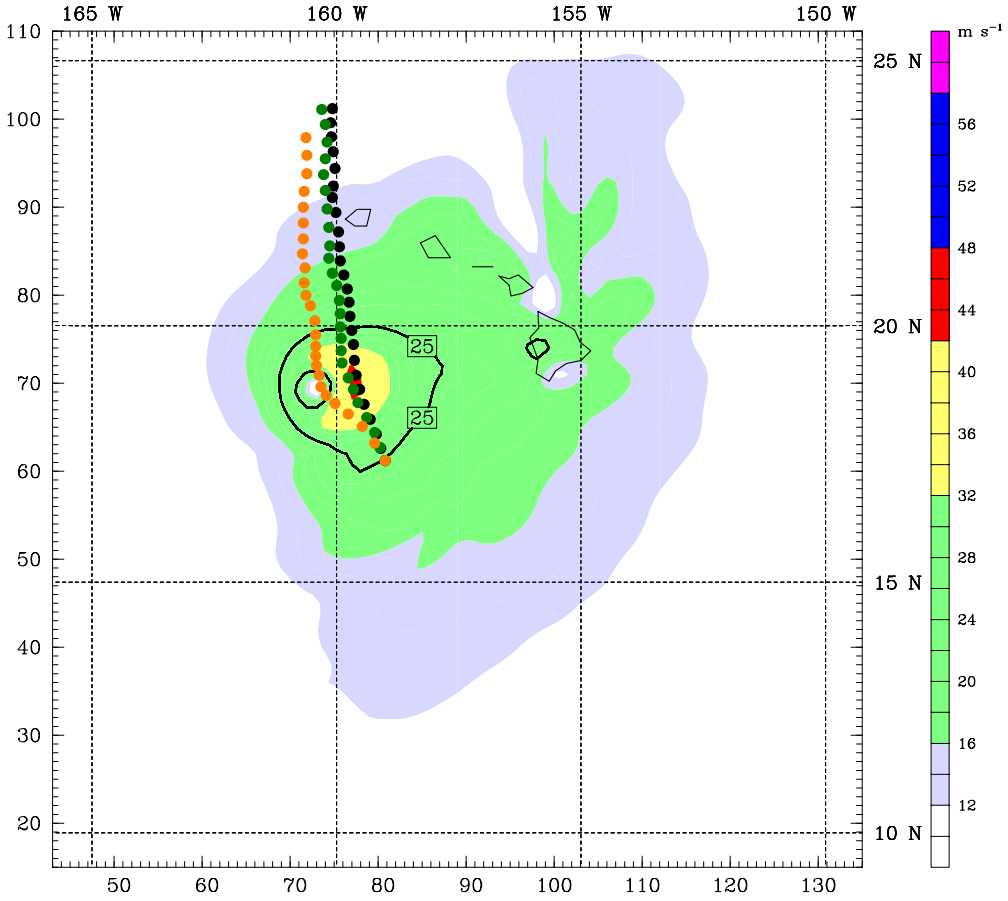

Fig. 7: *Cost function versus iteration for experiment $\mathcal{T}[\boldsymbol{X}]$. The total cost function (in thousands) and the individual parts of the cost function at $t = 0$ and 6 h are shown as solid, dotted, and dashed lines, respectively.*

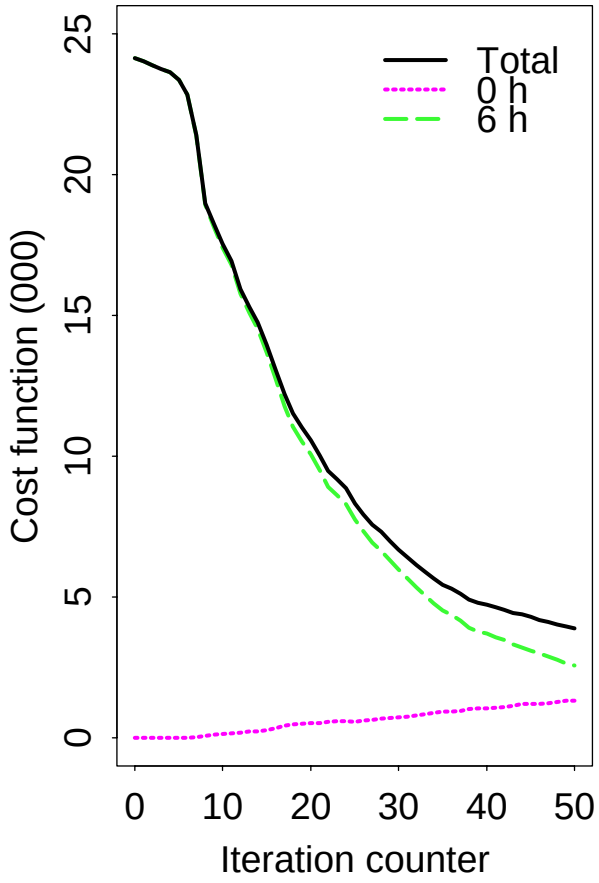

Fig. 8: *Profiles of rms difference in temperature and vector wind between model state and target for experiment $\mathcal{T}[\boldsymbol{X}]$. The components of J are converted into rms differences as described in the text. The rms differences after the minimization at $t = 0$ and 6 h are drawn with heavy dotted and dashed lines, respectively. The rms differences at the start of the minimization at 6 h are drawn with light dashed lines.*

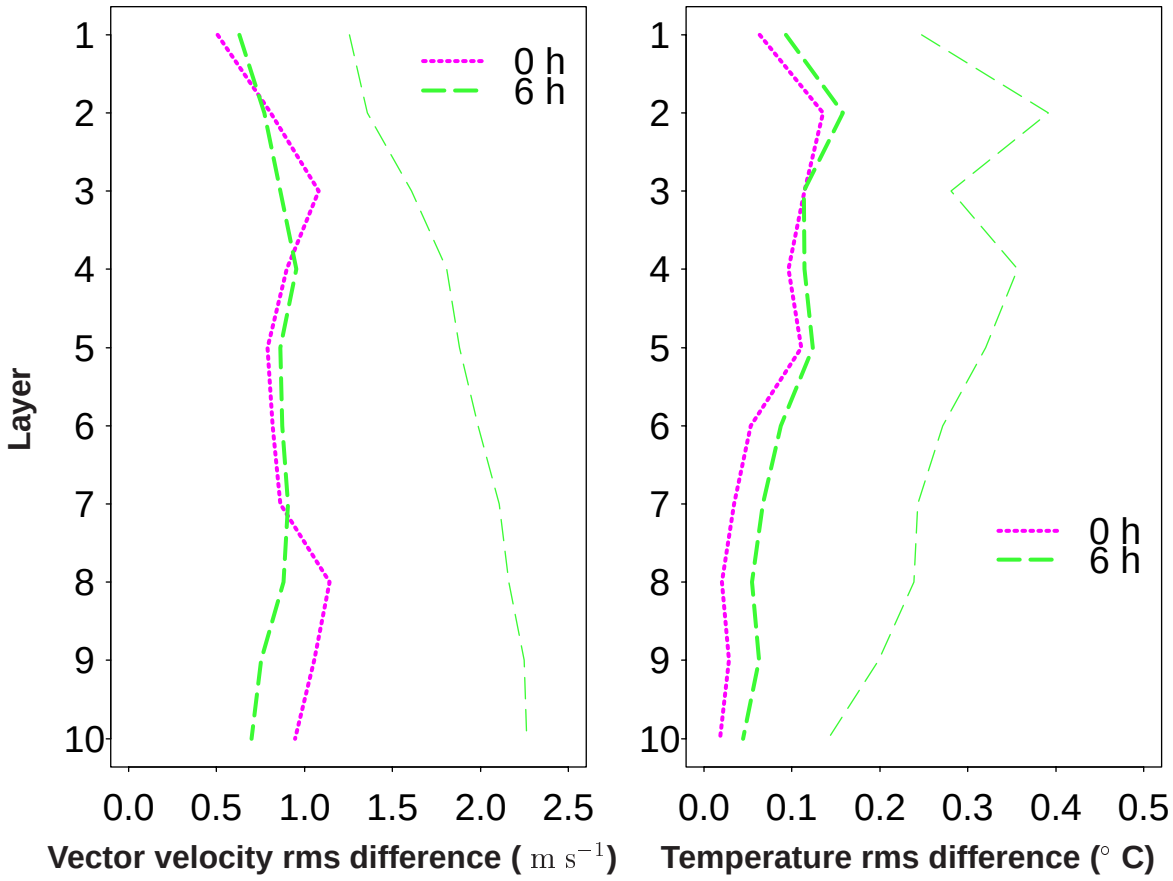

Fig. 9: *Structure of the perturbation for experiment $\mathcal{T}[\boldsymbol{X}]$. Horizontal slices of δT and $\delta \boldsymbol{V}$ are shown at 350, 650, and 950 hPa. Temperature in degrees C and wind speed in $\mathrm{m\ s^{-1}}$ and are color coded. Wind barbs are in kts.*

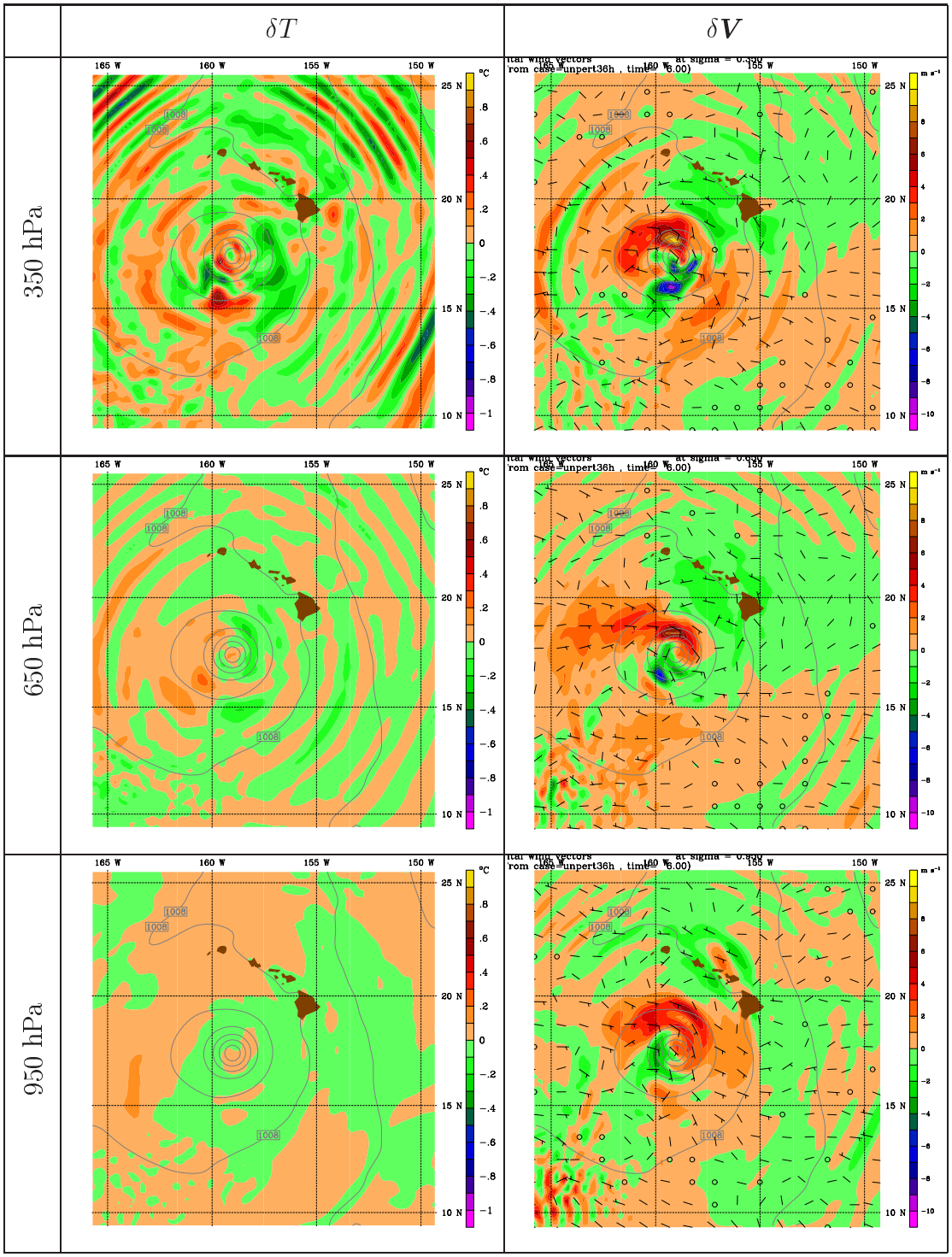

Fig. 10: *Evolution of the perturbation for experiment $\mathcal{T}[\boldsymbol{X}]$. Horizontal slices of δT, δw and $\delta \boldsymbol{V}$ are shown at 350, 650, and $950\ \mathrm{hPa}$ respectively, each at 2, 4, 6, and $8\ \mathrm{h}$. Temperature in degrees C, vertical velocity in $10^{-2}\ \mathrm{m\ s^{-1}}$, and wind speed in $\mathrm{m\ s^{-1}}$ are color coded. Wind barbs are in kts.*

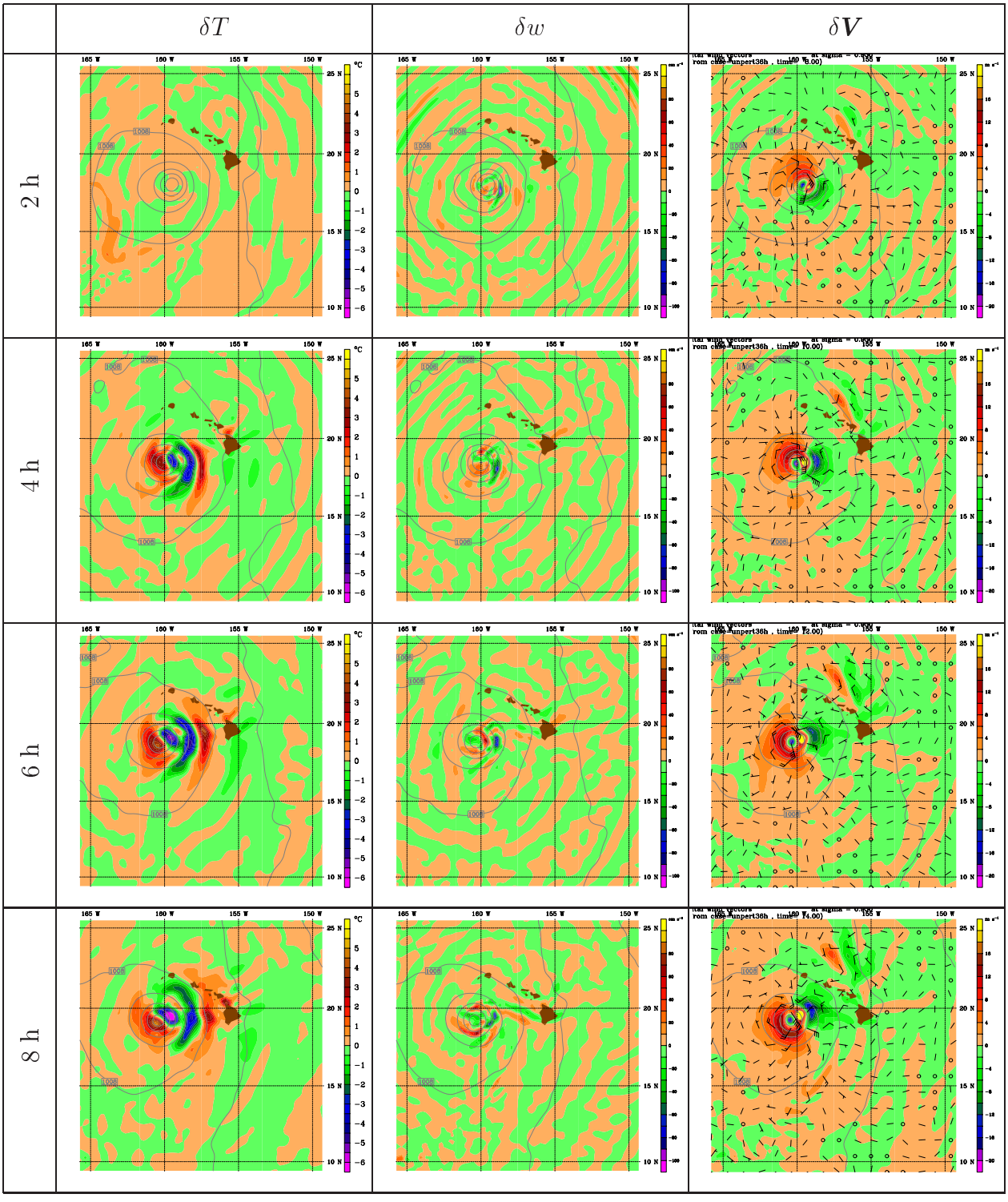

Fig. 11: *Evolution of the surface wind field for the unperturbed simulation* $\mathcal{U}$ *and for experiments* $\mathcal{T}[\boldsymbol{X}]$ *and* $\mathcal{C}[T]$*. Wind speed is color coded according to the Saffir-Simpson scale and the damaging wind contour* $25\ \mathrm{m\ s^{-1}}$ *is plotted at 4, 6, and* $8\ \mathrm{h}$*.*

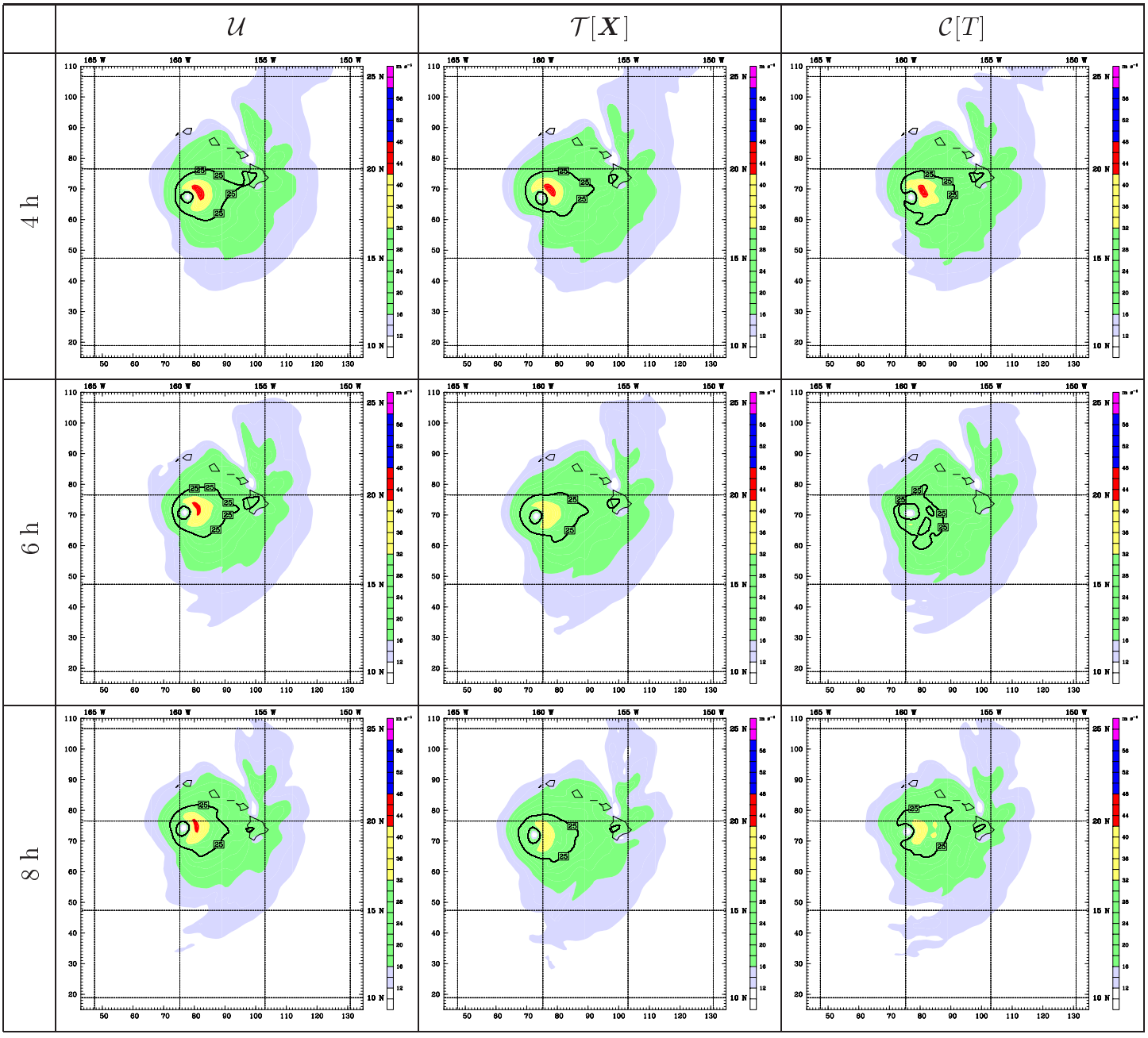

Fig. 12: *Cost function versus iteration for experiment $\mathcal{C}[T]$. As in Fig. 7, the total cost function (in thousands) and the individual parts of the cost function at $t = 0$ and 6 h are shown as solid, dotted, and dashed lines, respectively.*

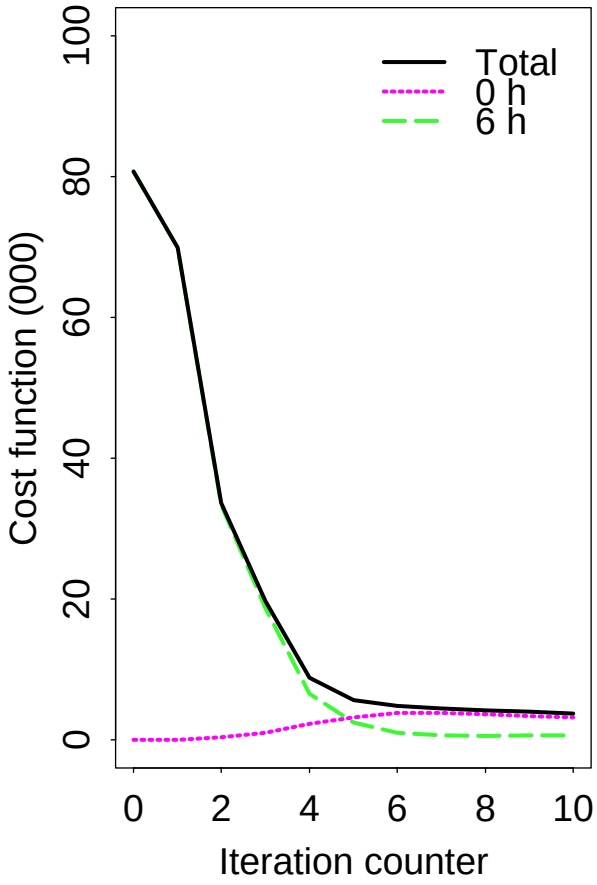

Fig. 13: *Profiles of rms difference in temperature for various $\mathcal{T}[\cdot]$ and $\mathcal{C}[\cdot]$ experiments. The components of J are converted into rms differences as described in the text. The rms differences for experiments using a full model state control vector are drawn with a full line, those with temperature only with a dotted line. Standard $\mathcal{T}[\cdot]$ and $\mathcal{C}[\cdot]$ experiments are drawn in black and magenta lines respectively, and alternative $\mathcal{C}[\cdot]$ experiments are drawn in green lines.*

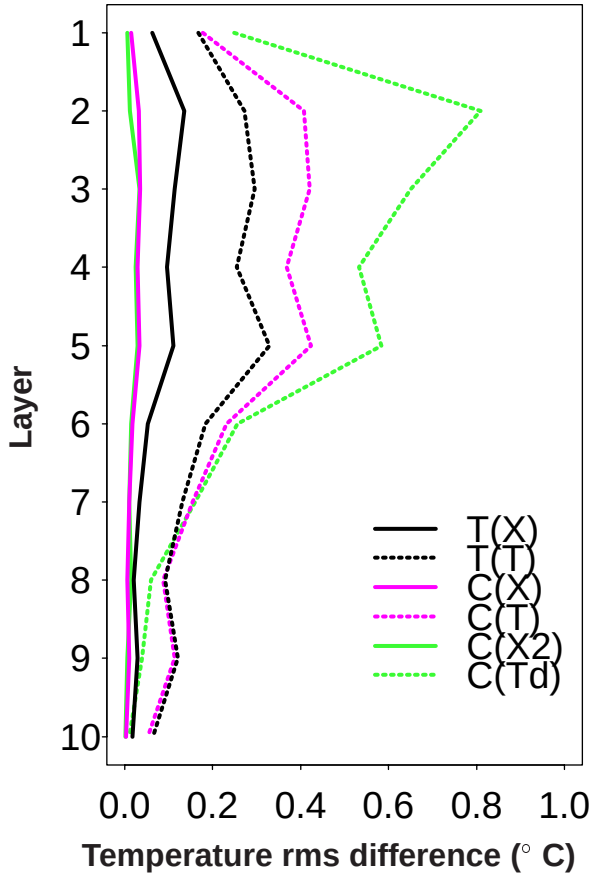

Fig. 14: *Structure of the perturbation for experiment $\mathcal{C}[T]$. Horizontal slices of δT are shown at 950, 650, and* 350 hPa*. Temperature in degrees C is color coded.*

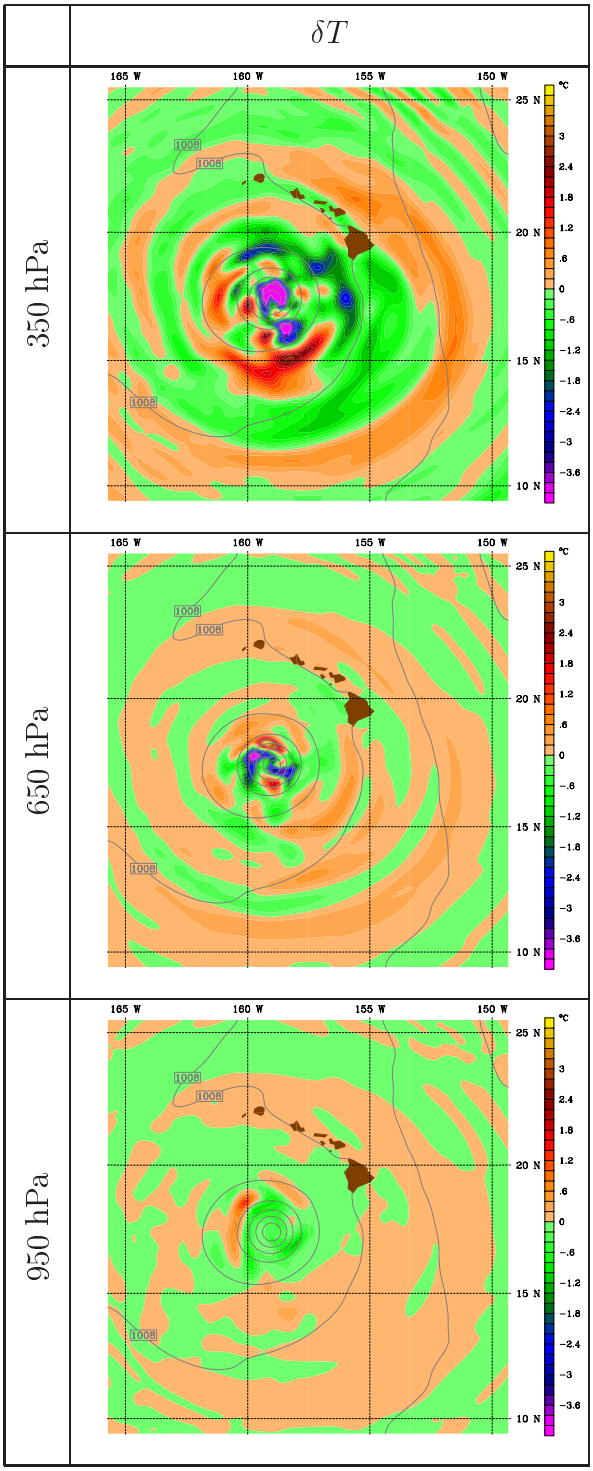

Fig. 15: *Evolution of the perturbation for experiment $\mathcal{C}[T]$. As in Fig. 10, horizontal slices of δT, δw and $\delta \boldsymbol{V}$ are shown at 350, 650, and 950 hPa respectively, each at 2, 4, 6, and 8 h. Temperature in degrees C, vertical velocity in 10^{-2} m s^{-1}, and wind speed in m s^{-1} are color coded. Wind barbs are in kts.*

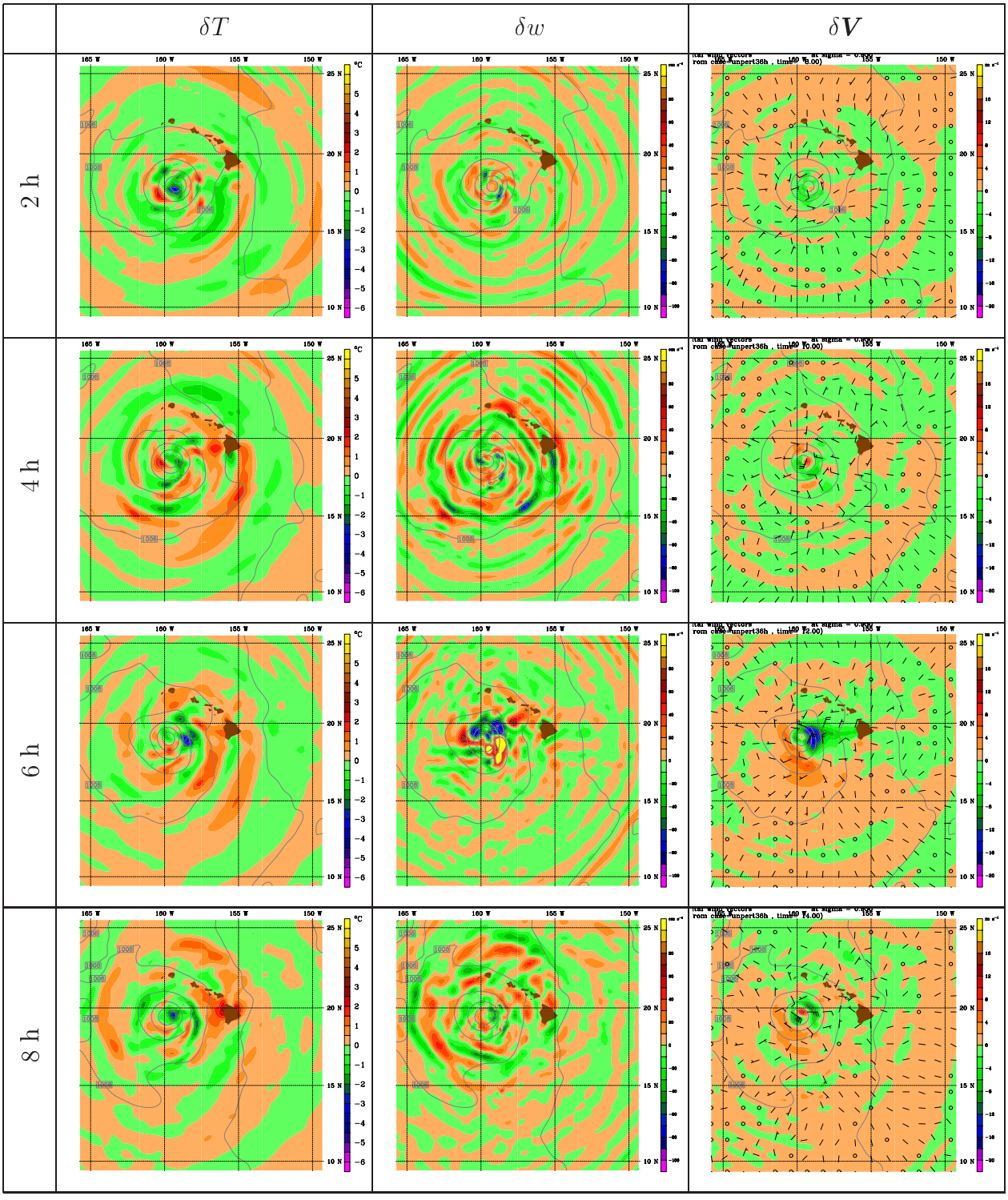

Fig. 16: *Structure of the wind perturbation $\delta \boldsymbol{V}$ for experiments $\mathcal{C}[\boldsymbol{X}]$ and $\mathcal{C}[\boldsymbol{X_2}]$. Horizontal slices are shown at 350, 650, and* 950 hPa. *Wind speed in* $\mathrm{m\ s^{-1}}$ *is color coded. Wind barbs are in kts.*

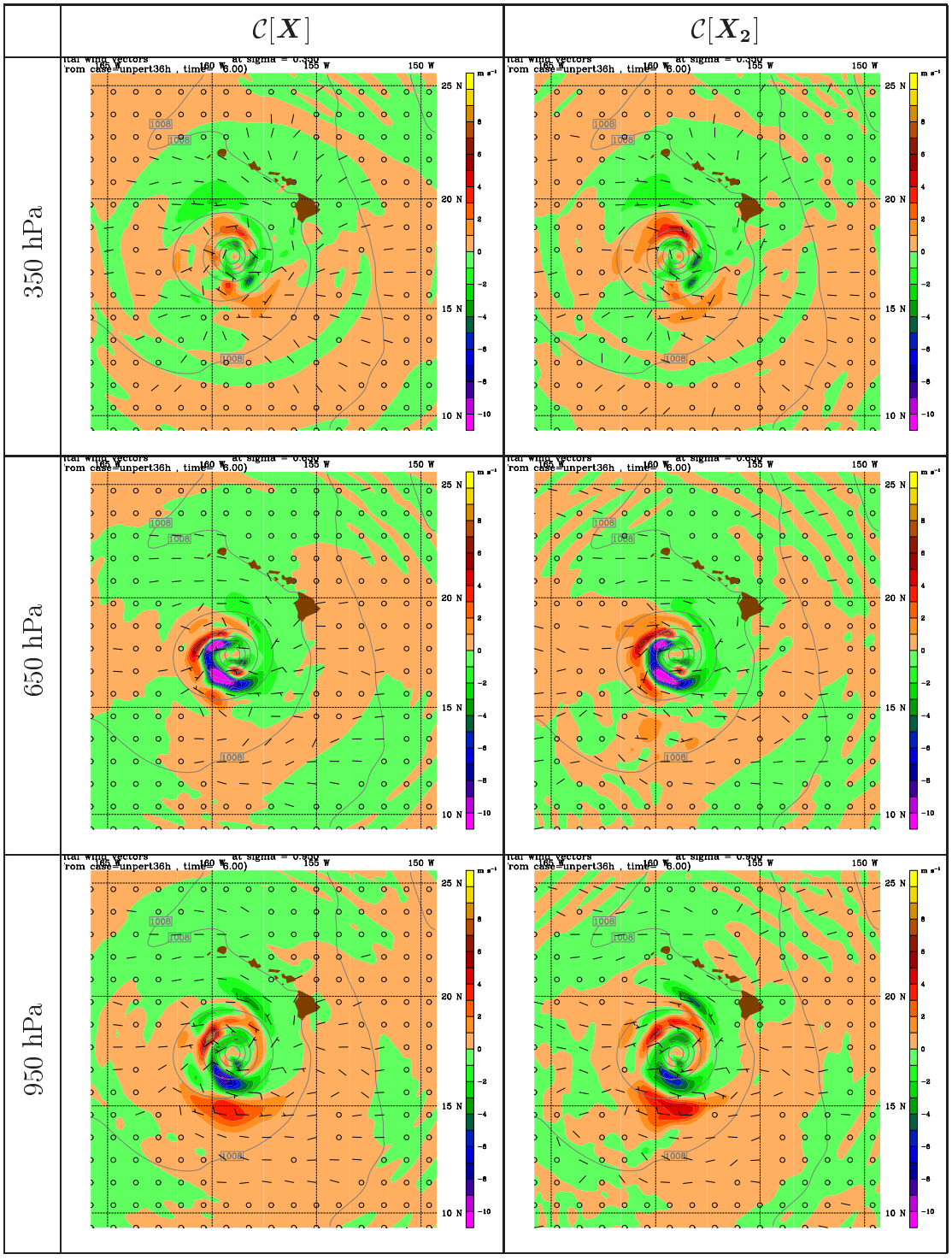

Fig. 17: *Perturbation temperature δT at 350 hPa for experiments $\mathcal{T}[\boldsymbol{X}]$ and $\mathcal{T}[T]$ (top row), $\mathcal{C}[\boldsymbol{X}]$ and $\mathcal{C}[T]$ (second row), and $\mathcal{C}[\boldsymbol{X_2}]$ and $\mathcal{C}[T_d]$ (bottom row). Temperature in degrees C is color coded. Note that the panel for $\mathcal{T}[\boldsymbol{X}]$ is the same field plotted in Fig. 9, but here the color scale has been chosen to match the other panels in this figure.*

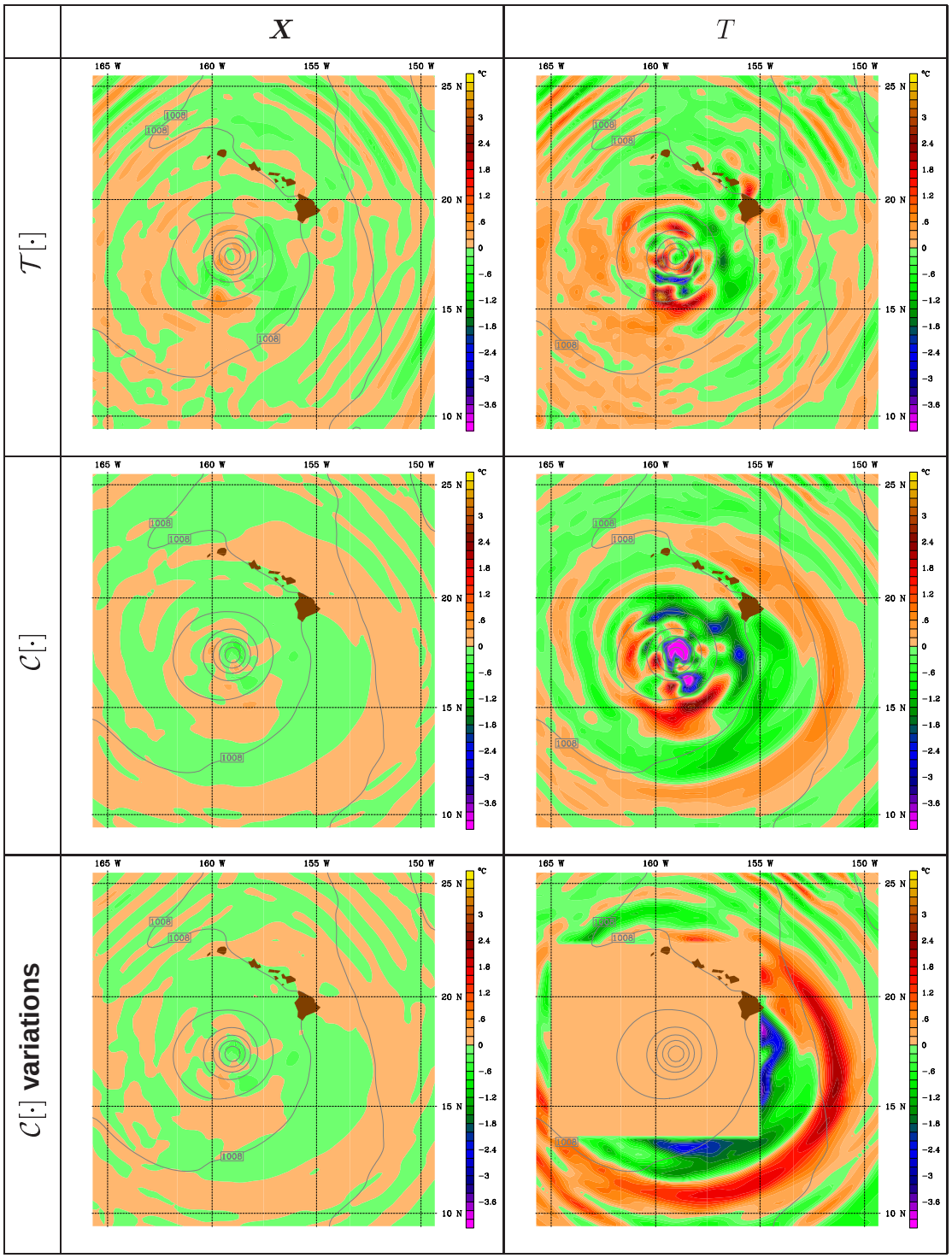

Fig. 18: *Surface wind field at* 6 h *for experiments* $\mathcal{T}[\boldsymbol{X}]$ *and* $\mathcal{T}[T]$ *(top row),* $\mathcal{C}[\boldsymbol{X}]$ *and* $\mathcal{C}[T]$ *(second row), and* $\mathcal{C}[\boldsymbol{X_2}]$ *and* $\mathcal{C}[T_d]$ *(bottom row). Wind speed is color coded according to the Saffir-Simpson scale and the damaging wind contour* 25 m s^{-1} *is plotted.*

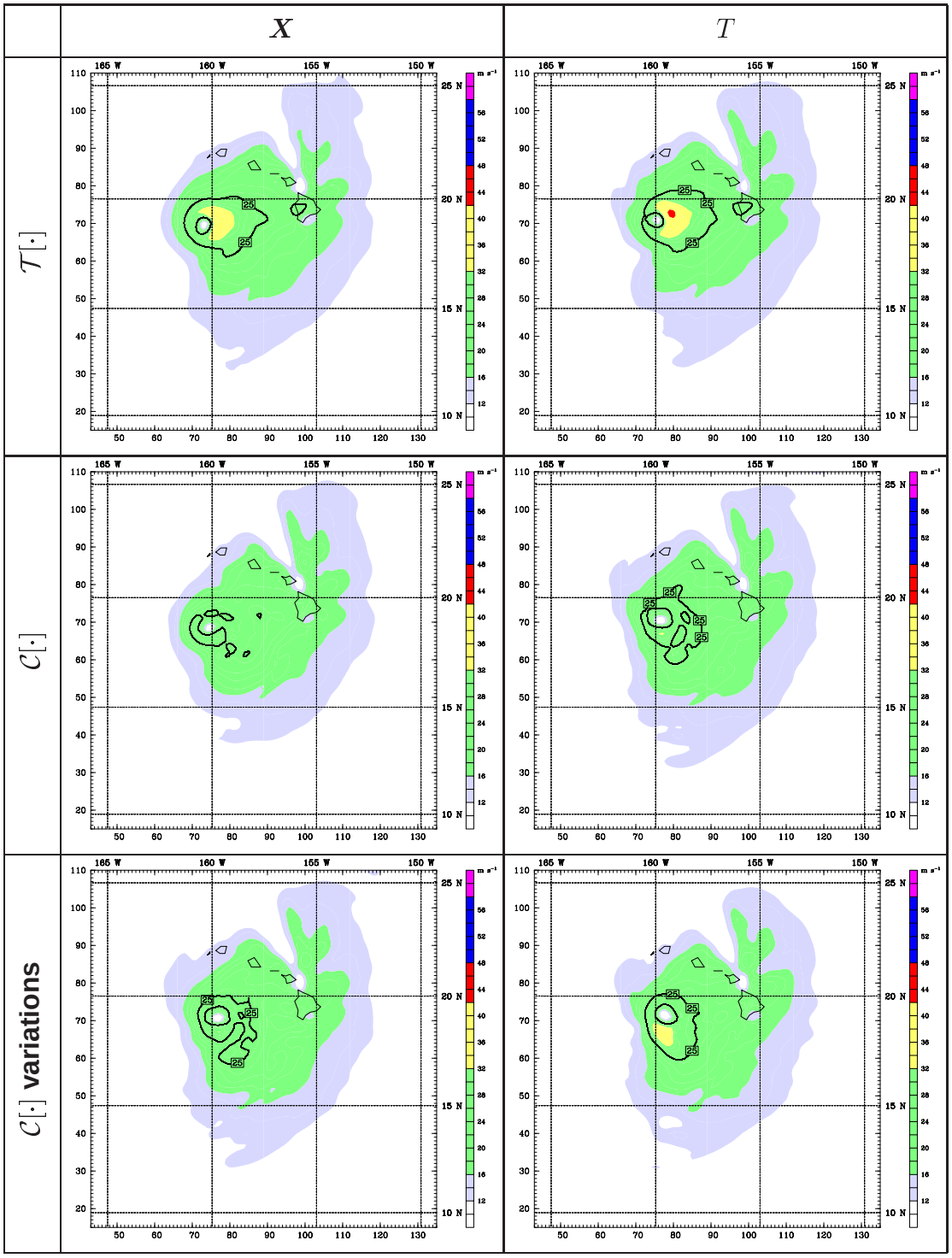

Fig. 19: *Evolution of the perturbation for experiment $\mathcal{C}[T_d]$. As in Fig. 10, horizontal slices of δT, δw and $\delta \boldsymbol{V}$ are shown at 350, 650, and 950 hPa respectively, each at 2, 4, 6, and 8 h. Temperature in degrees C, vertical velocity in 10^{-2} m s^{-1}, and wind speed in m s^{-1} are color coded. Wind barbs are in kts.*

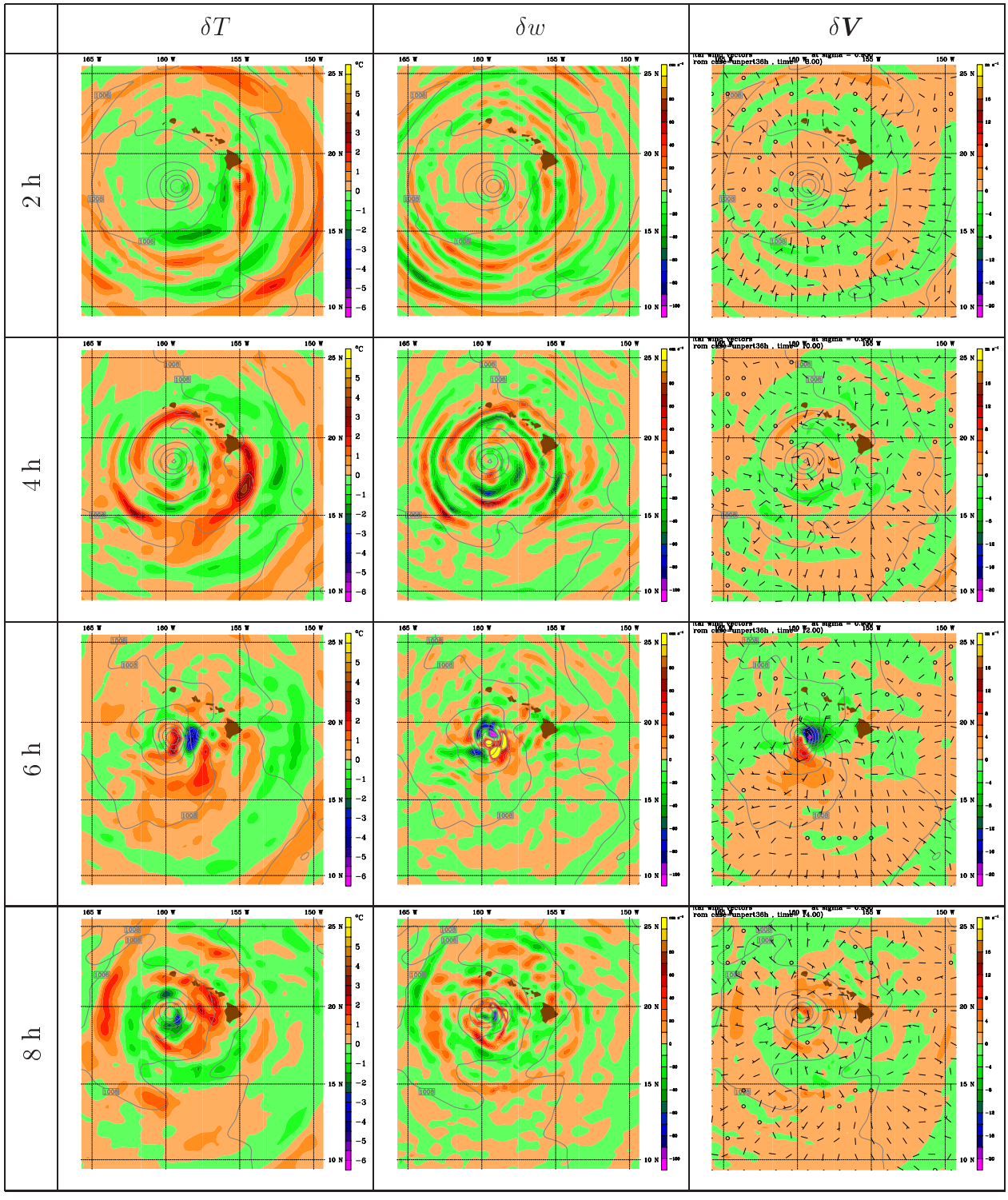

Fig. 20: *Perturbations for experiments with different control vectors. Wind at* 950 hPa *is plotted for experiment* $\mathcal{C}[\boldsymbol{V}]$*, vertical velocity at* 650 hPa *for* $\mathcal{C}[w]$*, specific humidity at* 650 hPa *for* $\mathcal{C}[q]$*, and perturbation pressure at* 950 hPa *for* $\mathcal{C}[p']$*. Wind barbs are in kts. Wind speed in* $\mathrm{m\ s^{-1}}$*, vertical velocity in* 10^{-2} $\mathrm{m\ s^{-1}}$*, specific humidity in* 10^{-3} $\mathrm{kg/kg}$ *and perturbation pressure in* hPa *are color coded.*

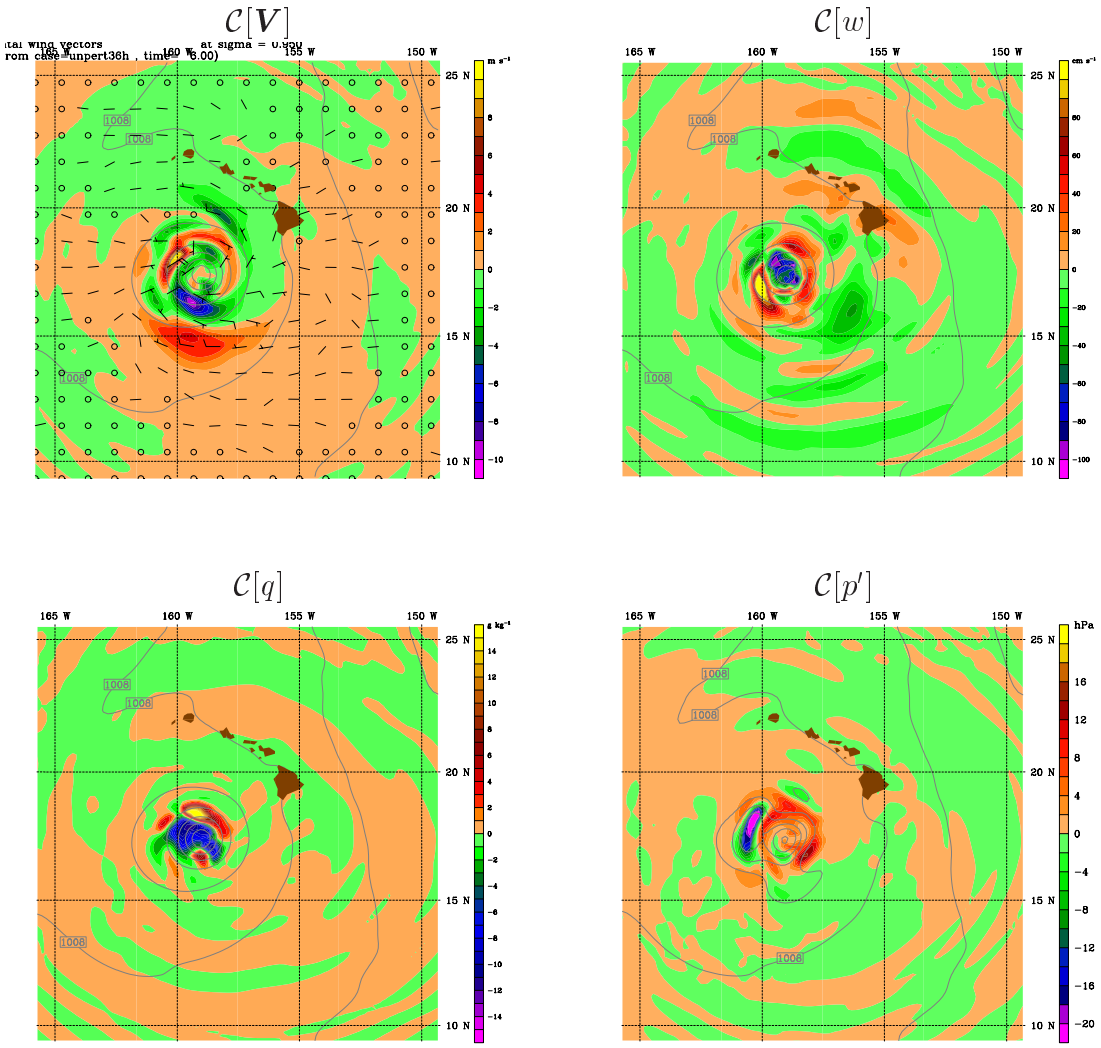

Fig. 21: *Surface wind field at* $6\ \mathrm{h}$ *for experiments* $\mathcal{C}[\boldsymbol{V}]$, $\mathcal{C}[w]$, $\mathcal{C}[q]$, *and* $\mathcal{C}[p']$. *Wind speed is color coded according to the Saffir-Simpson scale and the damaging wind contour* $25\ \mathrm{m\ s^{-1}}$ *is plotted.*

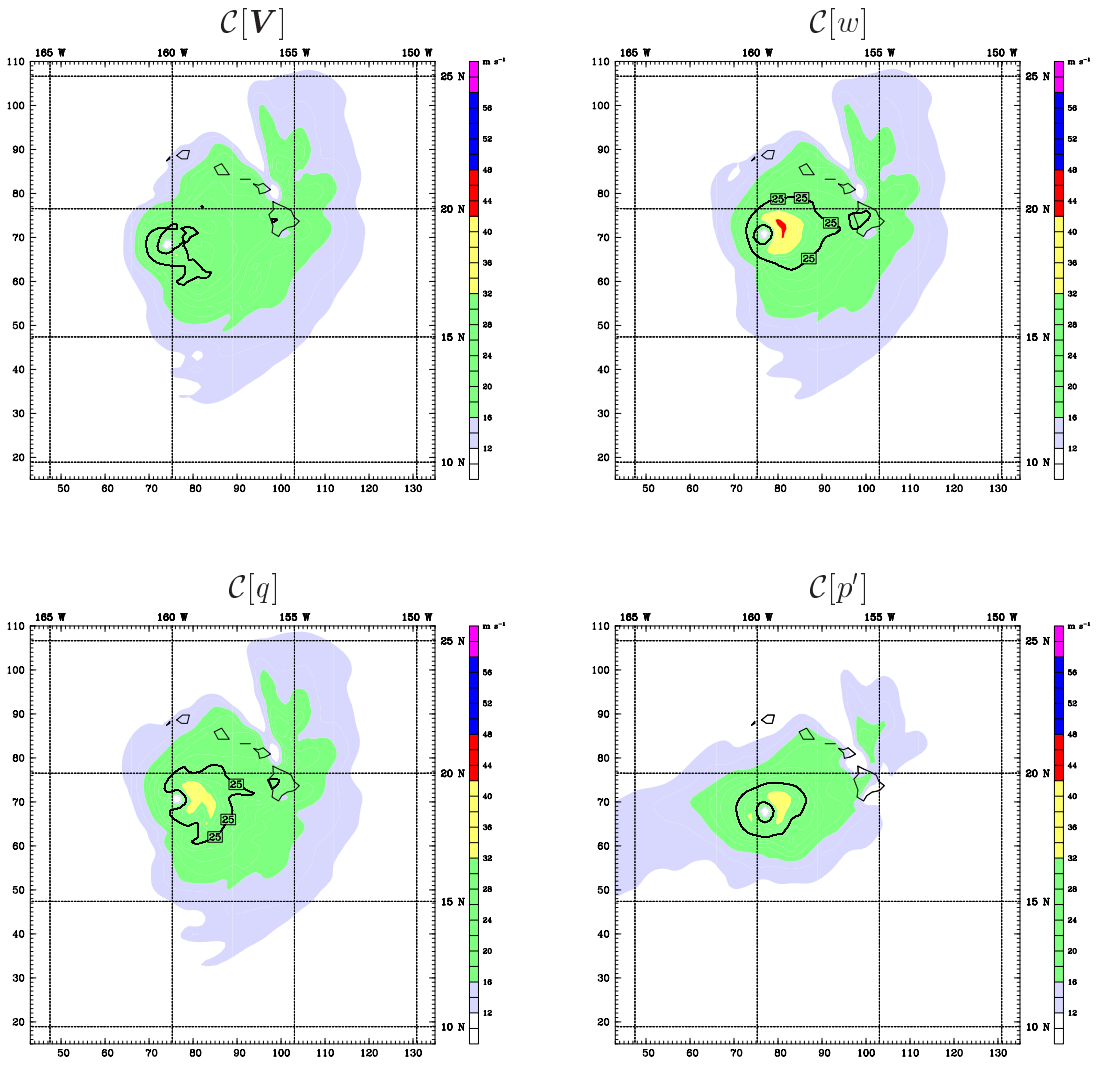

Fig. 22: *Structure of the perturbation for experiment $\mathcal{C}[T_a]$. As in Fig. 14, horizontal slices of δT are shown at 950, 650, and 350 hPa. Temperature in degrees C is color coded.*

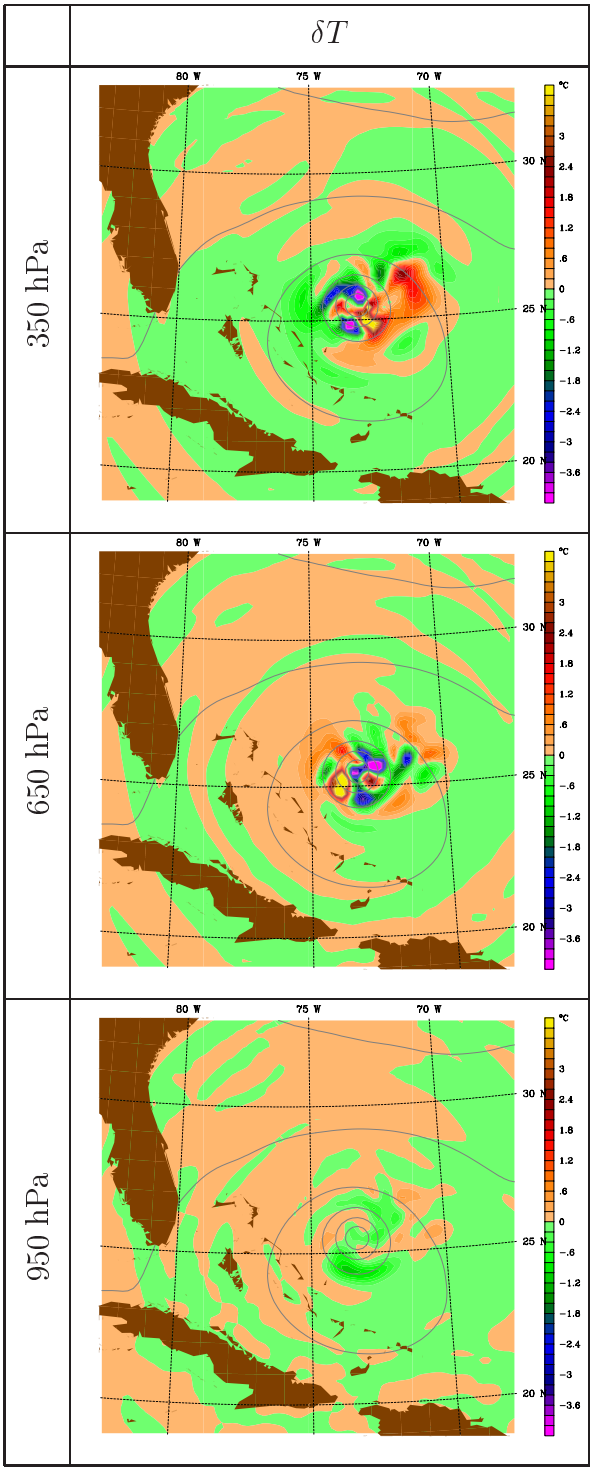

Fig. 23: *Evolution of the perturbation for experiment $\mathcal{C}[T_a]$. As in Fig. 10, horizontal slices of δT, δw and $\delta \boldsymbol{V}$ are shown at 350, 650, and 950 hPa respectively, each at 2, 4, 6, and 8 h. Temperature in degrees C, vertical velocity in 10^{-2} m s^{-1}, and wind speed in m s^{-1} are color coded. Wind barbs are in kts.*

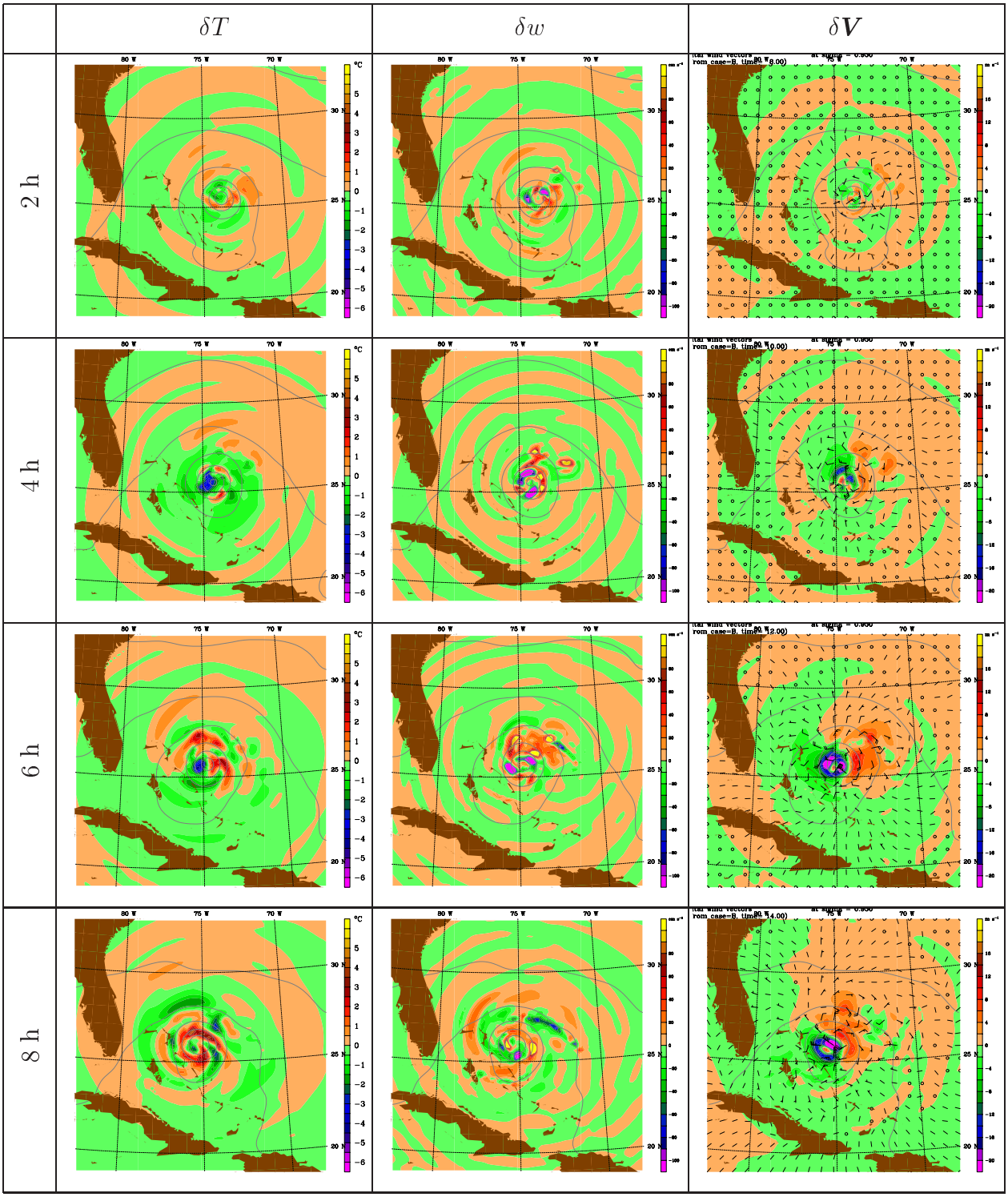

Fig. 24: *Evolution of the surface wind field for the unperturbed simulation* $\mathcal{U}_a$ *and for experiment* $\mathcal{C}[T_a]$*. As in Fig. 11, wind speed is color coded according to the Saffir-Simpson scale and the damaging wind contour* $25\ \mathrm{m\ s^{-1}}$ *is plotted at 4, 6, and* $8\ \mathrm{h}$*.*

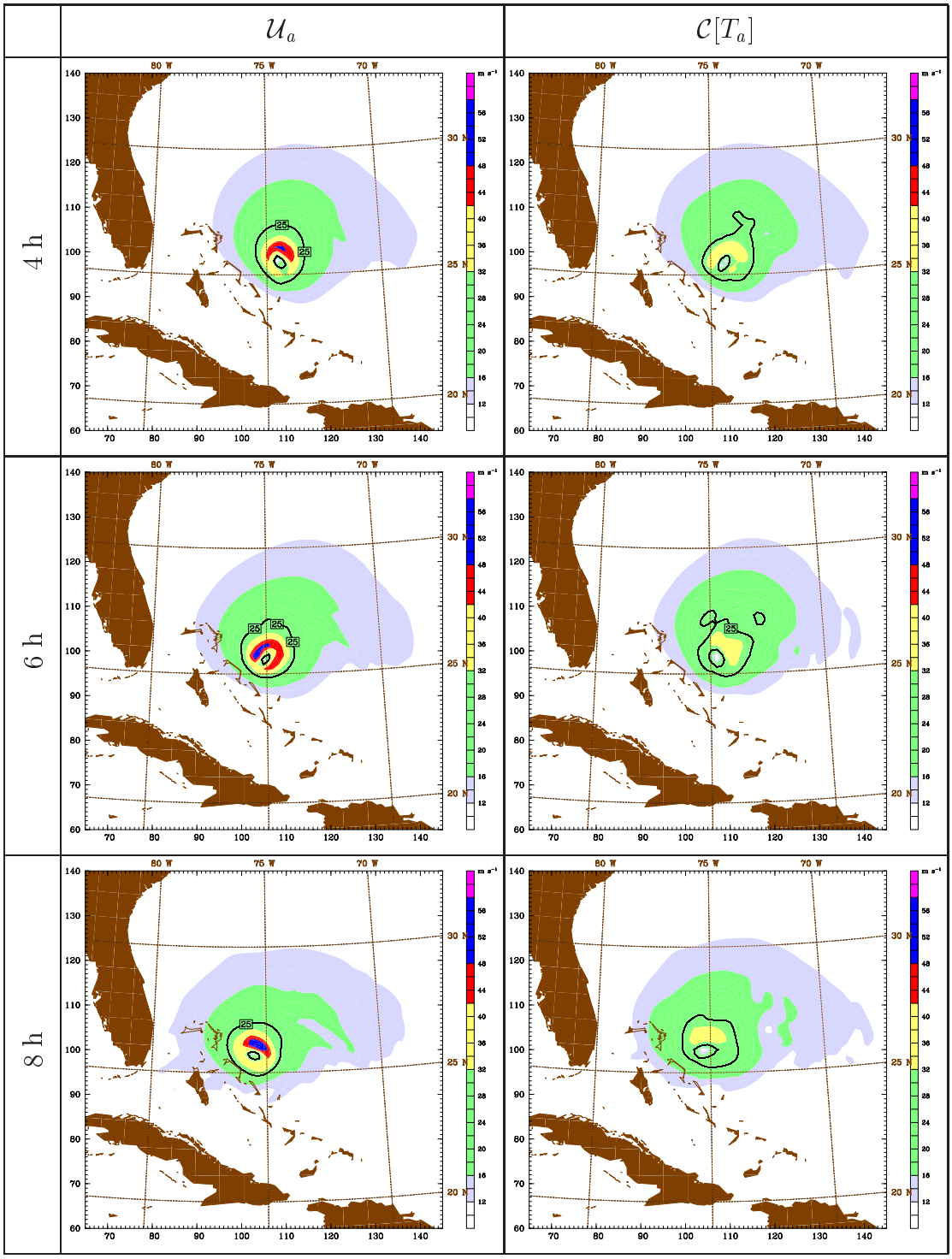

Fig. 25: *Refined property values and wind field at start of experiment $\mathcal{L}[T_a]$. Property values are unitless, but might be considered tens of thousands of dollars per square kilometer. Wind speed is color coded according to the Saffir-Simpson scale and the damaging wind contour $25\ \mathrm{m\ s^{-1}}$ is plotted.*

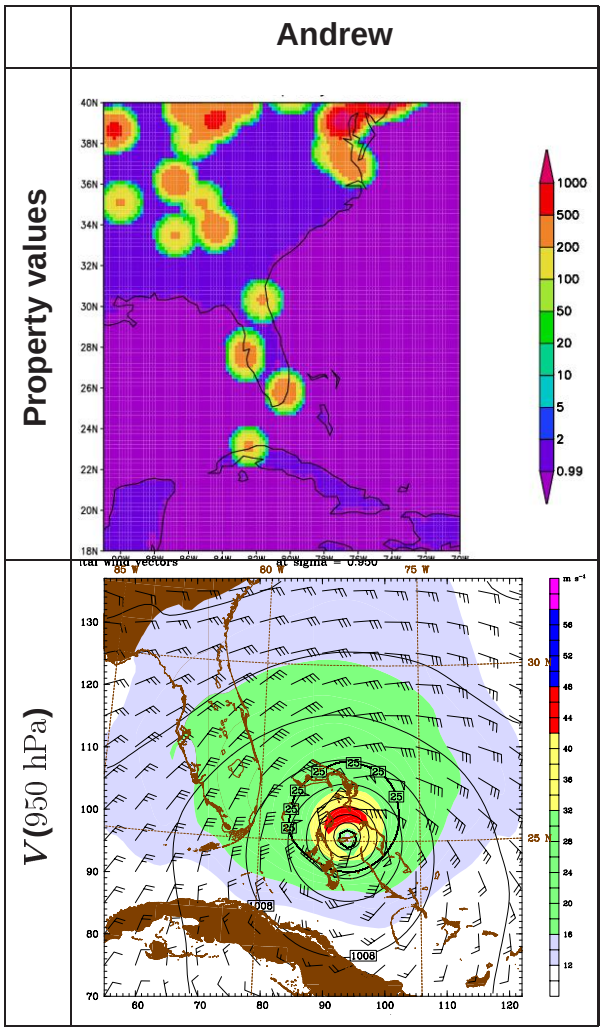

Fig. 26: *Structure of the perturbation for experiment $\mathcal{L}[T_a]$. As in Fig. 14, horizontal slices of δT are shown at 950, 650, and 350 hPa. Temperature in degrees C is color coded.*

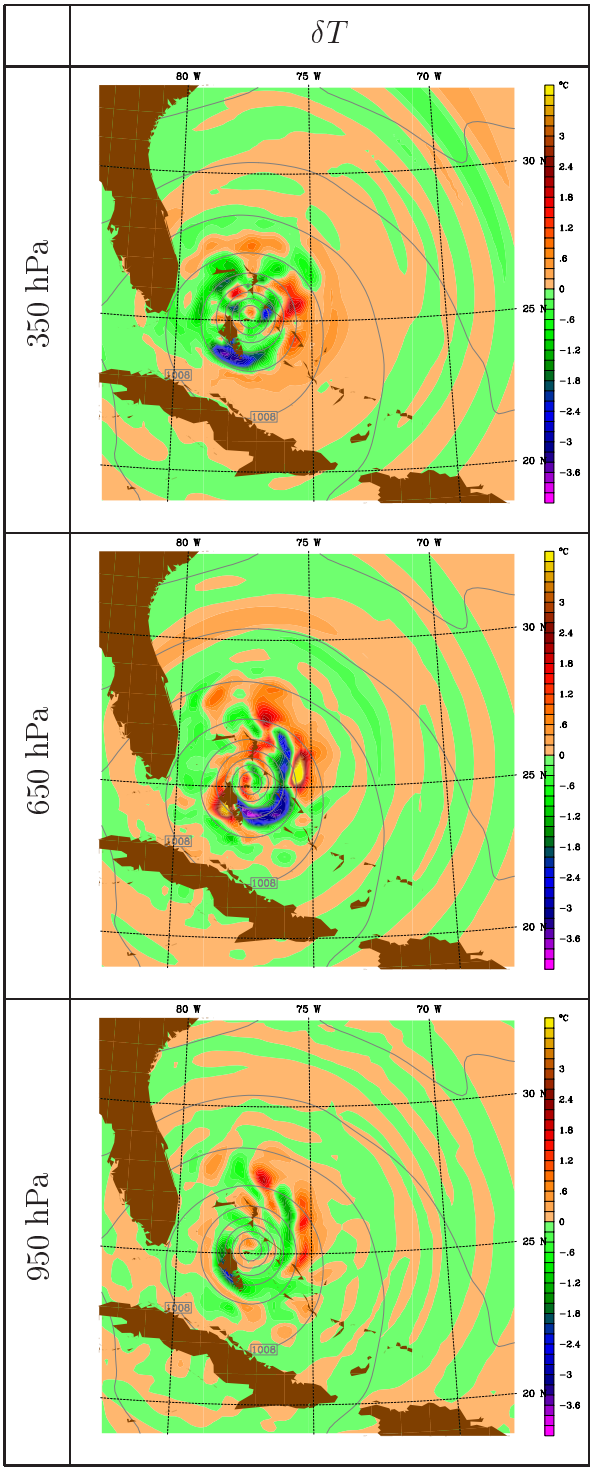

Fig. 27: *Evolution of the perturbation for experiment $\mathcal{L}[T_a]$. As in Fig. 10: Horizontal slices of δT, δw and $\delta \boldsymbol{V}$ are shown at 350, 650, and 950 hPa respectively, each at 2, 4, 6, and 8 h. Temperature in degrees C, vertical velocity in 10^{-2} m s^{-1}, and wind speed in m s^{-1} are color coded. Wind barbs are in kts.*

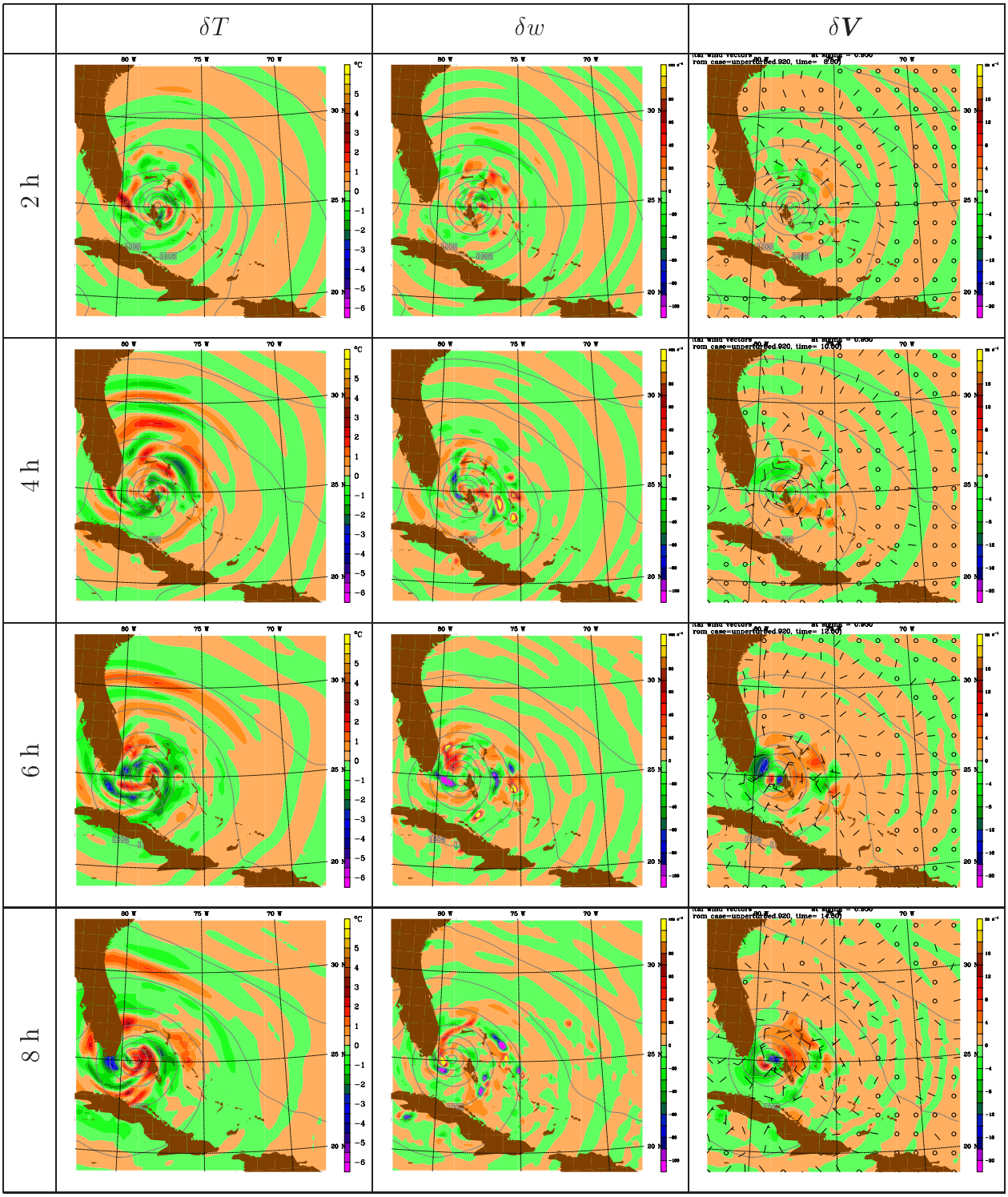

Fig. 28: *Evolution of the surface wind field for the unperturbed simulation* $\mathcal{U}_a$ *and for experiment* $\mathcal{L}[T_a]$*. As in Fig. 11: Wind speed is color coded according to the Saffir-Simpson scale and the damaging wind contour* $25\ \mathrm{m\ s^{-1}}$ *is plotted at 4, 6, and* $8\ \mathrm{h}$*.*

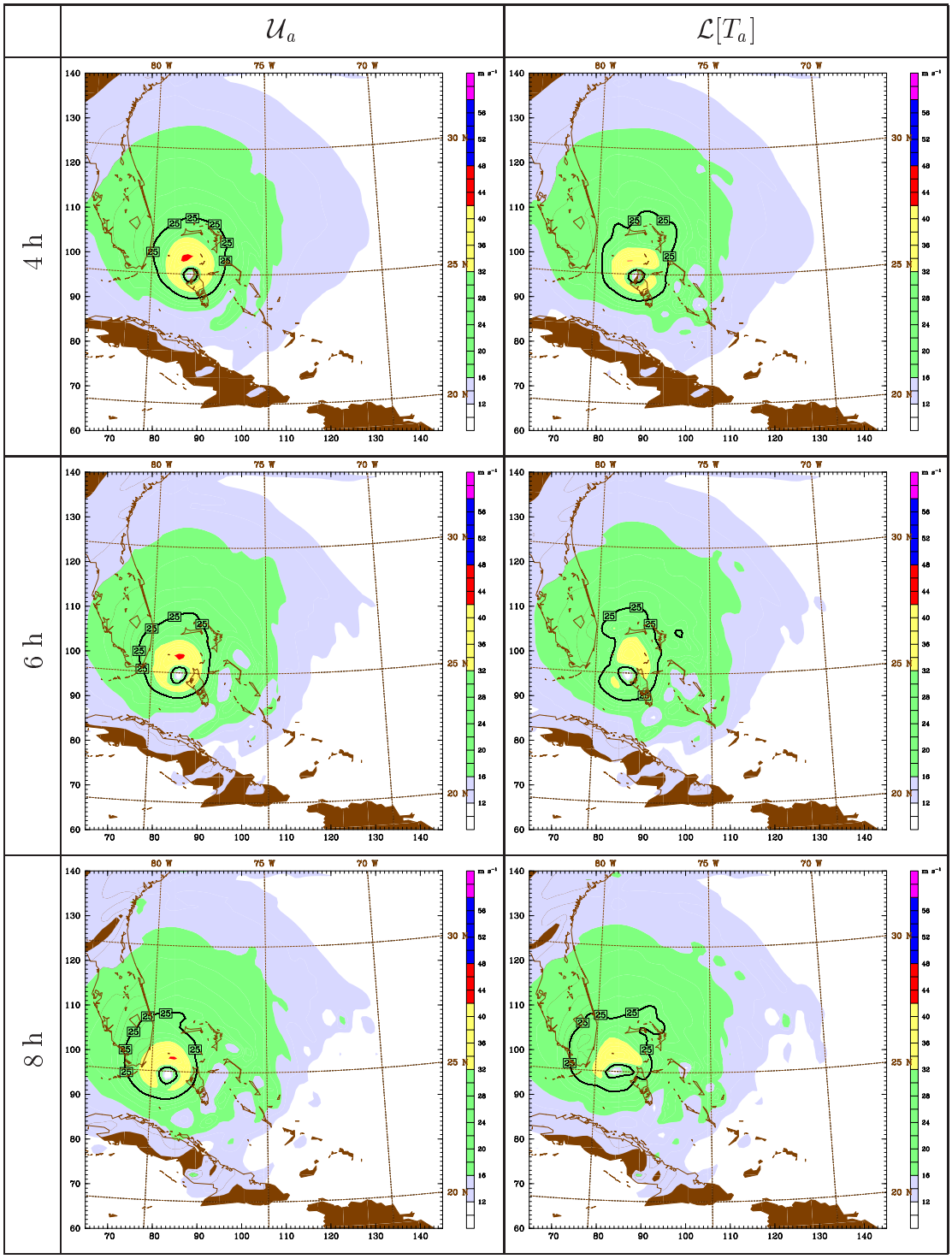

Fig. 29: *Surface wind field at* $6\ \mathrm{h}$ *for unperturbed and controlled for* $20\ \mathrm{km}$ *and* $7\ \mathrm{km}$ *simulations. The* $20\ \mathrm{km}$ *simulations use simpler and the* $7\ \mathrm{km}$ *simulations use more complex physical parameterizations than in all preceeding cases. Wind speed is color coded according to the Saffir-Simpson scale and the damaging wind contour* $25\ \mathrm{m\ s^{-1}}$ *is plotted.*

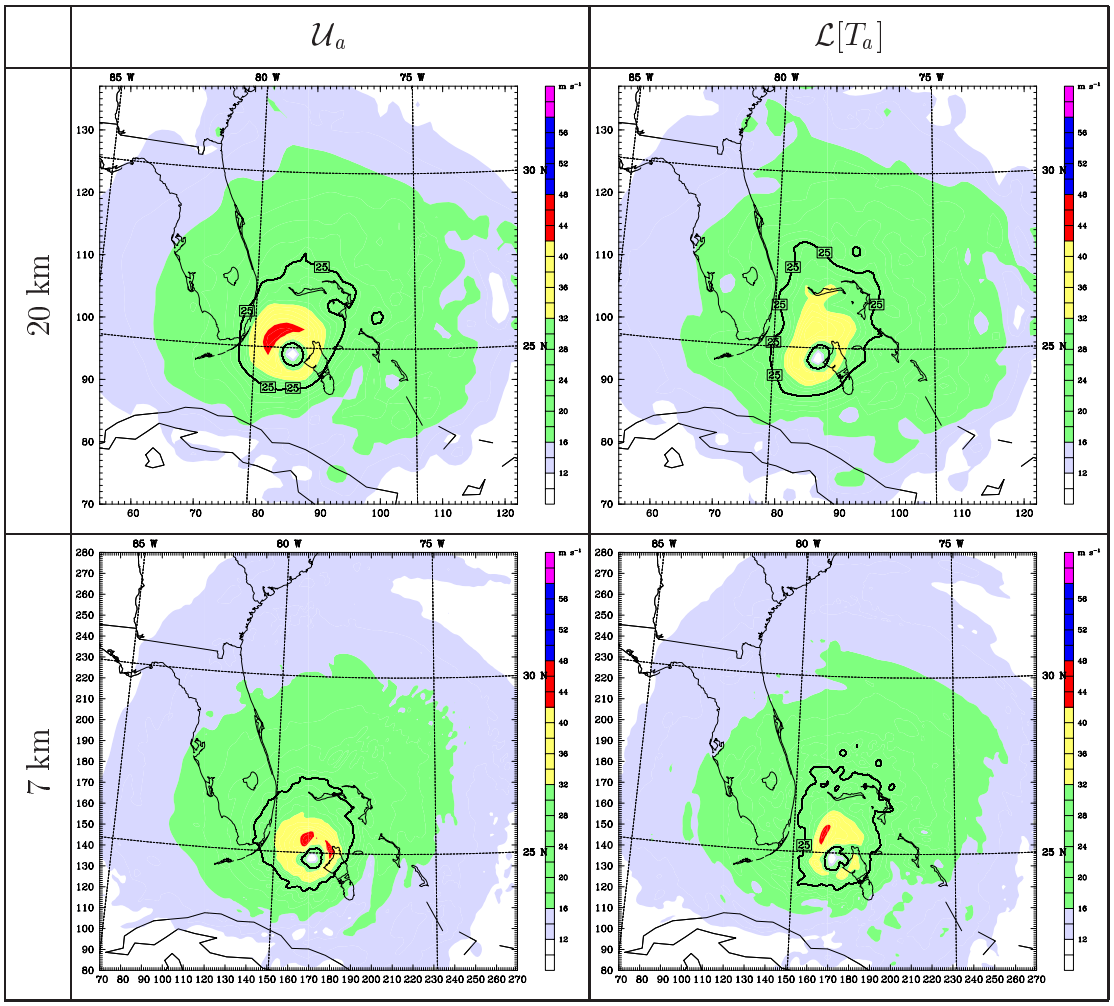

Fig. 30: *Profiles of rms difference in temperature for various $\mathcal{C}[\cdot]$ preliminary experiments for Iniki. The components of J are converted into rms differences as described in the text. The rms differences for an experiment using a full model state control vector is drawn with a full magenta line, that with temperature only with a dotted magenta line. Both of these are at 40 km resolution. Results for donut experiments at both 20 and 40 km are shown as solid and dotted green lines. For reference experiment $\mathcal{C}[T_d]$ is plotted in black.*